On the generation of surfable ship waves in a circular pool: Part I

Physical background & Wave pool design

M.A. de Schipper
M.Sc. Thesis

Graduation committee:
Prof. dr. ir. G.S. Stelling
Prof. dr. ir. M.J.F. Stive
Dr. ir. H.J. de Koning Gans
Dr. ir. A.J.H.M. Reniers
Dr. ir. W.S.J. Uijttewaal
Ir. M. Henriquez
Ir. R.J. Labeur
Ir. J.S.M. van Thiel de Vries

June 22, 2007
Delft University of Technology
Faculty of Civil Engineering and Geosciences
Section of Hydraulic Engineering and Environmental Fluid Mechanics

Preface

This thesis concludes the Master of Science program at the section of Hydraulic Engineering and Environmental Fluid Mechanics of the Faculty of Civil Engineering and Geosciences at Delft University of Technology.

In spring 2006, Sierd de Vries and I were contacted by Professor Stive about an Australian surfboard manufacturer, Greg Webber, searching assistance in the development of a new invention; a circular pool with surfable waves generated by ship-like hulls. Soon the contact was established and it turned out to be an interesting research project.
The results of research are documented in two theses. The author strongly recommends the thesis of Sierd de Vries, *'On the generation of surfable ship waves in a circular pool: Part II, the application of stereo photo technique measuring water surface elevation and surface flow velocities'*.

The author gratefully acknowledges the suggestions of the graduation committee, Prof. G.S. Stelling, Prof. M.J.F. Stive, Dr. H.J. de Koning Gans, Dr. A.J.H.M. Reniers Dr. W.S.J. Uijttewaal, Ir. M. Henriquez, Ir. R.J. Labeur and Ir. J.S.M. van Thiel de Vries. Furthermore the valuable comments and enthusiasm of Steven Schmied, Australian project manager of the wave pool, are acknowledged.

The author is very grateful for the support of all people at the Fluid Mechanics Laboratory at the faculty of Civil Engineering and Geosciences, the Ship Hydromechanics Laboratory at the faculty of Mechanical, Maritime and Materials Engineering and WL|Delft Hydraulics in the realisation of the physical model tests.

Special thanks go out to my parents, family and friends. You all have been supportive in so many ways.

Finally, Sierd, thank you for sharing your enthusiasm and valuable comments.

Matthieu de Schipper

Delft, June 2007

Summary

Surfing as a sport is growing. Locations with good surfing conditions are limited and therefore crowded. The growing interest for the sport led to a new concept, surf pools. Surf pools mimic good surfing conditions found along the coast.
This thesis is about the technical feasibility of a new surf pool concept invented by Greg Webber. Webber's invention is to creating surfing waves in a circular pool by towing ship-like hulls around. The hulls are towed along the outer wall of the pool and waves generated by these hulls propagate inwards and break on an island in the middle of the pool. The waves break around the island which theoretically leads to endless surf rides. The initial design as suggested by Webber is based on a pool diameter of 200 m and a water depth of 3 m. The objective of his design to generate 2 m high waves for intermediate to expert surfers.

The objective of this study are twofold: 1) understanding the physical phenomena in such a wave pool and 2) evaluating and amending the initial design.

Because of the lack of knowledge about ship induced waves in such an enclosed environment, a physical and a numerical model study are carried out.

Various hull sizes are towed in a towing tank and the surface elevations are measured and analyzed. From this physical model study it was concluded that the wave pattern behind a hull is the result of a complex interference pattern and is easily disturbed when the velocity beside the hull becomes large. The difficulties of wave generation by a hull therefore lie in the return currents. The magnitude of the return flow is a function of the blockage K, the percentage of the cross section of the pool blocked by the hull.
In case the blocking and the velocity are too large, water accumulates in front of the hull and the wave field behind the hull is disturbed, the so-called the trans-critical regime.
In case of a smaller blocking and velocity, a full wave pattern can develop since the velocities beside the hull are small. The hull is then towed at a sub-critical speed.
Maximum wave heights are found when to towing a hull at the boundary of sub-critical and supercritical regime. The maximum wave height H is limited by the water depth h. A maximum wave height of 0.3 times the water depth ($H = 0.3\ h$) is found in the physical model.

The current state-of-the-art numerical models are incapable to model a wave pool with ship-like hulls in all its aspects yet. The complexity of the problem lies in the combination of moving objects, both sub-critical and trans-critical flow, breaking waves and the accompanying currents.

The initial wave pool design is evaluated, and it was concluded that the water depth h of 3 m is insufficient to generate the desired 2 m waves. Moreover, the suggested high blockage of 15% will cause a translation wave and large return currents, since the hull is towed in the trans-critical domain.
Therefore an amended design is presented. Water depth is increased to 7 m and the generation area is enlarged to reduce the blocking to 5%. The large generation area causes a weak return flow and therefore less turbulence in the pool. In such a cross section it is

technically possible to generate 2 m surfable waves by towing a hull in the sub-critical range. The wave form and angle at breakpoint are ideal for intermediate to expert surfers.

Contents

List of Symbols and Abbreviations

Symbol	*Definition*
A_c	Cross sectional area of the channel [m^2]
A_{flow}	Cross sectional area of the flow [m^2]
A_s	Cross sectional area of the ship [m^2]
B_c	Channel width at the waterline [m]
$B_{f.s.}$	Width of the free surface [m]
B_s	Ship width (Beam) [m]
C	Wave phase speed [m/s]
C_0	Wave phase speed near the hull [m/s]
C_g	Wave group speed [m/s]
D_s	Ship draft [m]
EMF	Electro-magnetic field meter; velocity measurement device
$F_{r,d}$	Froude depth number ($\frac{V_s}{\sqrt{gh}}$)[-]
$F^*_{r,d}$	Froude number relative to the return flow ($\frac{V_s+U_r}{\sqrt{gh}}$) [-]
g	Gravitational constant [m/s^2]
H	Wave height [m]
h	Water depth [m]
H_b	Wave height at breakpoint [m]
h_b	Water depth at breakpoint [m]
h_{t_+}	height of the positive translation wave in front of the hull w.r.t. SWL [m]
K	Blockage ($\frac{A_s}{A_c}$) [-]
K_r	Wave height refraction factor [-]
K_s	Wave height shoaling factor [-]
L	Wave length featherlet waves[m]
L_b	Wave length at breakpoint [m]
L_e	Entry length (length from the bow to the parallel cross section along the hull) [m]
L_o	Wave length on deep water [m]
L_s	Ship length [m]
L_t	Wave length transverse waves [m]
n	Ratio between group and phase velocity [-]
SWL	Still Water Level
T	Wave period featherlet waves [s]
U_r	Return current beside the hull [m/s]
U_{t_+}	Depth averaged mean velocity in the positive translation wave [m/s]
v	Hull speed relative to the water [m/s]
V_h	Hull speed with relation to the bank [m/s]
V_s	Hull speed relative to the water [m/s]
V_{tow}	Input velocity of the towing tank carriage [m/s]
y	the distance to the bow perpendicular to the sailing line ($y > 0$) [m]
z_a	Water level depression beside the hull [m]

Greek symbols

Symbol	*Definition*
α	Steepness of the slope [-]
α_1	Wave height calculation, shape coefficient [-]
α_2	Wave height calculation, speed dependency exponent [-]
α_u	velocity distribution coefficient [-]
β	Relative free surface width [-]
ΔQ	Discharge stored in translation wave
Φ	Wave angle at the point of interest [-]
Φ_b	Wave angle at breakpoint [-]
Φ_o	Wave angle at near the hull [-]
ϕ	Featherlet wave angle w.r.t. the sailing line [-]
γ	Breaker depth coefficient [-]
η	Surface elevation w.r.t. SWL [m]
λ	Wave length [m]
θ	Interference angle w.r.t. the sailing line [-]
ρ	Density of water [kg/m^3]
ξ	Iribarren breaker type parameter [-]
∇	Vector divergence operator [1/m]

1 Introduction

Surfing as a sport has grown tremendously over the last decades. Locations with good surfing conditions are limited and therefore crowded. With the growing understanding of what makes a good surfing spot, it is possible to improve or create good surfing conditions with man-made structures at sea or on land.
The necessities for surfing are on one hand waves, and on the other hand a bottom topography transforming the waves in the right shape. Several artificial surf reefs are planned and built at locations lacking the latter over the last years. For locations where both waves and the right topography are lacking, like inland, surfable waves can be created in a surf pool.
There are several different wave pools around the globe, with waves varying from barely surfable to almost perfect. Waves in these conventional wave pools are generated by sucking water into a caisson and releasing it.
Australian surfboard manufacturer, Greg Webber, invented a new wave pool concept using waves generated by a ship (called ship waves from hereon). The technical feasibility of this wave pool concept is the main subject of this report.

1.1 Surfing and good surfing conditions

A pool mimics the surf conditions as found at a location with a good surfing conditions. Surfing is paddling into a wave, standing up and riding the unbroken wave face. Close to the boundary between the broken and unbroken part of the wave, the breakpoint, the wave face is at its steepest. Surfers stay close to this breakpoint since only there the wave face enables the surfer to overcome gravity and drag to perform maneuvers.

The shape of the breaking wave required for surfing is related to the steepness of the face. The steepest waves form a cavity under the plunging jet, a so called plunging breaker (see figure 1.1), and surfers try to ride within this cavity. These plunging breakers are desirable for experienced surfers.
If the cavity under the plunging jet becomes small and the roller crumbles from the crest a wave is called spilling. A spilling wave is less steep and therefore more suited for beginning surfers.

Figure 1.1: Surfers surfing a spilling breaker in a wave pool *(left)* and a plunging wave outdoors. PHOTOGRAPHS BY JASON PHILLIPS AND NICK BORELLI.

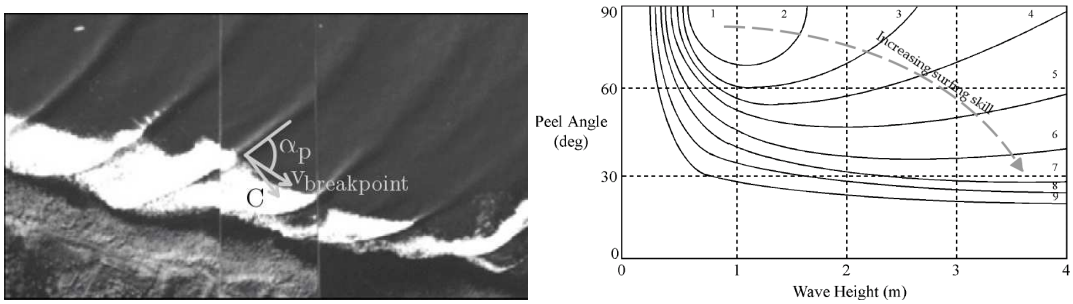

Figure 1.2: Aerial photograph indicating the peel angle and the surfing skill classification. after Hutt et al. (2001)

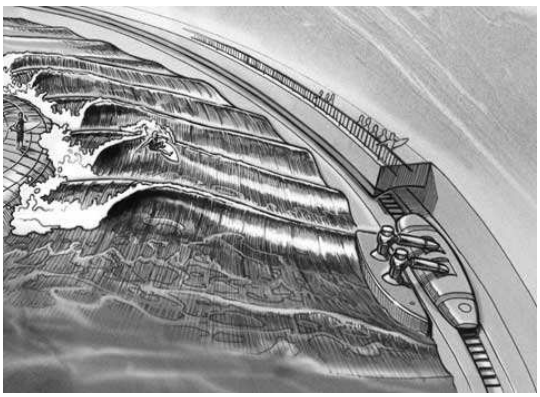

Figure 1.3: Artist impression Liquid Time Wave Pool. ILLUSTRATION BY LEW KEILAR.

The breakpoint moves along the wave crest, which is called peeling, and the surfer tries to match this pace. The ability to maintain in front of the breaking part of the wave even if the breakpoint advances fast, is part of the surfer's skill.
The peeling behavior is often expressed by the peel angle, the angle between the wave crest and the path of the breakpoint, which can be estimated from a top view of the water surface (see figure 1.2). Large peel angles imply a slowly moving breakpoint, which is easier to surf. The breakpoint velocity, which is the minimum velocity for a surfer to remain on the unbroken part of the wave, is hence given by :

$$v_{breakpoint} = C\frac{1}{\sin\alpha_p}. \tag{1.1}$$

With $v_{breakpoint}$, the breakpoint velocity [m/s],
C, wave speed [m/s] and
α_p, the peel angle [-].

Since the wave speed C at breakpoint is dependent on the wave height, the velocity of the breakpoint is expressed as a function of the peel angle and wave height,
$v_{breakpoint} = f(H, \alpha_p)$.

The difficulty of a wave is expressed in three parameters; 1) the wave height, 2)the breakpoint velocity and 3) the breaker shape. The surfer skill classification in Hutt et al. (2001) describes the surfer's skill level required as function of the wave height H and the peel angle α_p, thus taking into account the first two parameters. The classification of Hutt (based on the work of J.R. Walker in the early seventies) rates surfer skill from 1 to 9, where 1-3, 4-6 and 7-9 represent beginners, intermediate and expert surfers respectively (see figure 1.2).

Starting point in the design for a wave pool, is creating an exciting ride. This implies creating spilling or plunging waves of 1 m or higher and peel angles of 30 to 60 degrees.

1.2 Liquid time concept

The Liquid Time Wave Pool (called wave pool from hereon) concept, invented and copyrighted by Greg Webber, strives to produce surfing waves by using ship waves. The project aims are wave heights up to 2 m to facilitate wave conditions for surfers with intermediate to expert level.
An initial design of the wave pool is based on a circular pool with an outer diameter of 200 m. Several hulls are towed along the outer wall generating a wave pattern propagating inwards. Waves are intended to break on a 1:6 slope starting 13 m from the outer wall (see figure 1.3 to 1.5).
The breakpoint moves in a circular path, and nearly endless surf rides are therefore possible. The hulls are tapered, being 3 meters wide at the still water level and 4 meters wide at the pool floor. The hulls are 12 m long and each hull is supposed to generate multiple surfable waves.
By reversing the towing direction, both left and right hand peeling waves can be generated. The hull profile is hence designed symmetrical.

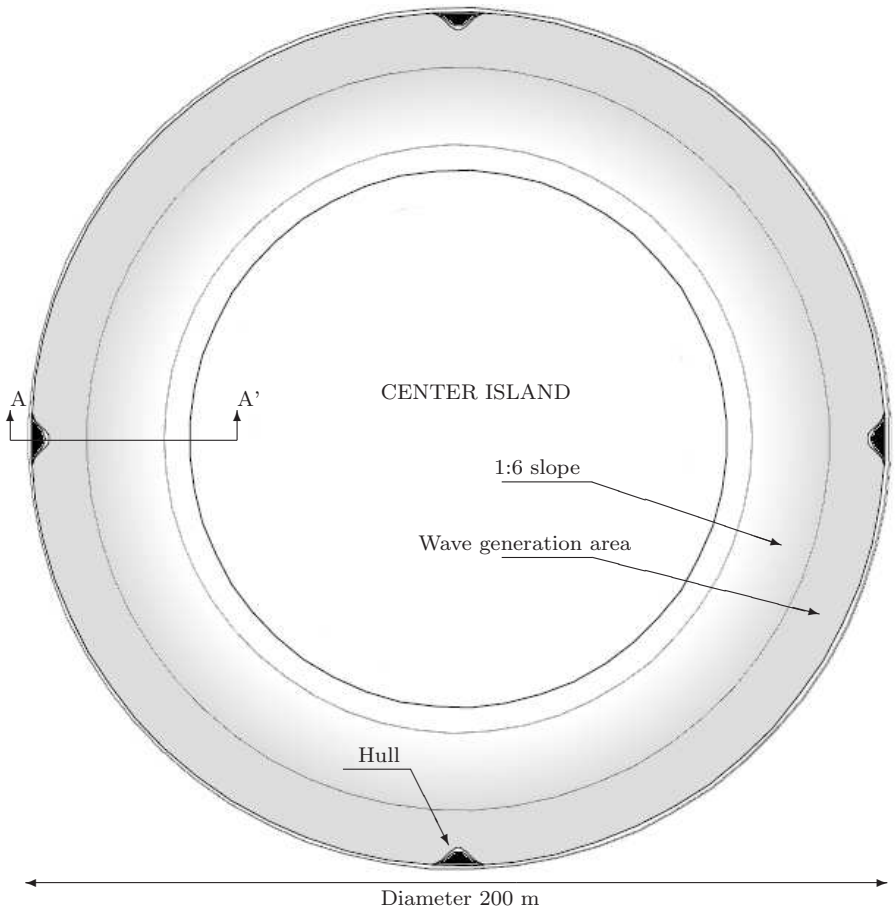

Figure 1.4: Top view initial design wave pool.

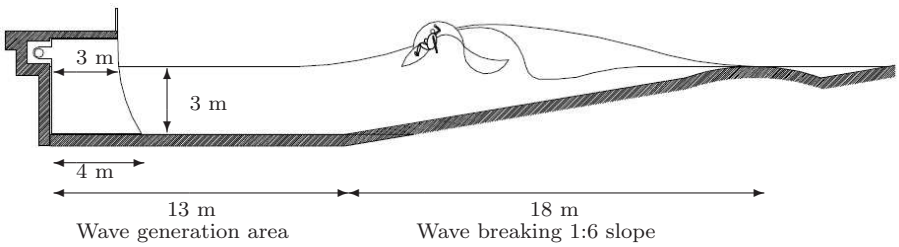

Figure 1.5: Cross section A-A' initial design wave pool.

1.3 Research objective

Wave angle, length and height in an ordinary wave pool with caissons can be fine tuned and are user defined. In a 'ship-wave' wave pool these variables are interrelated and a function of the velocity of the hull, and the cross sectional area of the hull and pool combined (as shown in the upcoming chapter). The movement of the hull generates beside the desired wave field a return flow. The return flow hinders the surfer paddling into the wave. The size of the wave generation area is a mayor factor in the size of the return currents. **Main objective of this study is to comprehend the physical phenomena which occur in a circular wave pool with ship-like hulls as wave makers. This includes investigating the hull velocity required to achieve 2 m waves and the design of the cross section of the pool, such that it is optimized for surfing.** The findings form the basis of an evaluation and optimization of the current (initial) wave pool design as well as giving guidelines for a further modeling.

1.4 Outline report

After this introductory chapter, the possibilities and difficulties for such a wave pool are investigated by looking at theory in chapter 2. Next the results of a physical model are discussed in chapter 3. The possibilities of a numerical model of a wave pool are the subject of chapter 4. The verification of the initial design as well as improvements are discussed in chapter 5. The conclusions of this study will be presented in chapter 6.

2

Wave theory

The existing theory of waves generated by ships and waves breaking on a bottom topography is explained in this chapter. The theory forms the basis of the interpretation of the outcomes of physical modeling as well as the evaluation of the design later on.

2.1 Ship waves

Consider an object moving through a straight canal with a constant velocity V_s. Water is then displaced from in front of the object to behind the object, as follows from continuity. The local increase in water velocity beside the hull causes a corresponding water level depression along the object. This return current and water level depression are called the primary wave system of a moving object.
The flow curving around the object causes velocity and pressure gradients in the flow. These gradients generate small waves that radiate into the fluid, much like a stone thrown in the water. Since this disturbance point moves, the radial waves will interfere with each other behind the vessel. The resulting interference pattern is the secondary wave system and can be seen behind a ship or any moving obstacle as a typical V-pattern (see figure 2.1). In the following sections both wave systems will be elaborated on, starting with the primary wave.

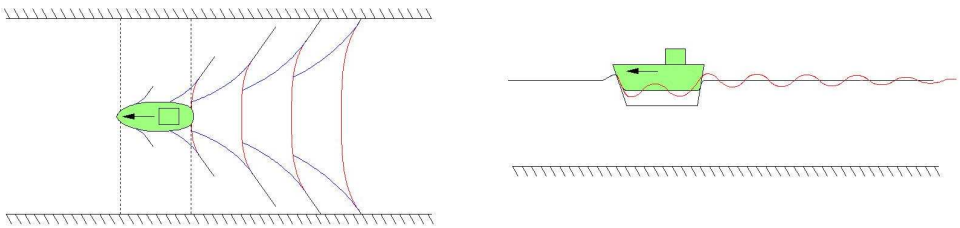

Figure 2.1: Primary and secondary wave system for a moving vessel in top and side view.

Primary wave

The primary wave of a vessel in a canal is schematised by defining a water level depression along side the ship z_a and the corresponding return current U_r. The magnitude of these variables can be calculated using mass and momentum conservation. For the calculation it is convenient to change from reference frame. This means that instead of a vessel moving with V_s through a canal, a new reference frame is chosen on the vessel such that the vessel has no speed and the water flows by with V_s (figure 2.2). This transformation (Galilean transformation) is valid as long as no energy loss (due to e.g. sidewalls or turbulence) is relevant in the calculation.

The balance equations in this reference frame lead to the following set of equations (assuming incompressibility of water).
Volume balance, given by:

$$A_c V_s = (A_c - A_s - z_a(B_c - B_s))(V_s + U_r). \tag{2.1}$$

Momentum balance, given by:

$$\frac{1}{2}\rho V_s^2 + \rho g h = \frac{1}{2}\rho \alpha_u (V_s + U_r)^2 + \rho g (h - z_a). \tag{2.2}$$

With V_s, the velocity of the hull [m/s],
A_c, the cross sectional area of the canal [m^2],
A_s, the cross sectional area of the ship [m^2],
B_c, the width of the canal [m],
B_s, the width (*beam*) of the ship [m],
z_a, the water level depression beside the hull [m],
U_r, the depth averaged return current beside the hull [m/s],
h, the water depth [m],
ρ, the density of the water [kg/m^3] and
α_u, the velocity distribution coefficient (equation (2.6)) [-].

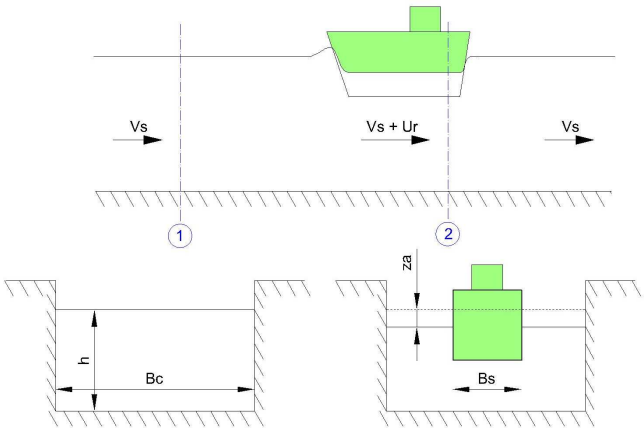

Figure 2.2: Primary wave schematisation.

The schematisation is valid when the width and depth of the canal are the same order of magnitude as the width and depth of the hull, so assumption of a constant the water level depression z_a is valid.

It is common practice (Lamb (1932)) to express the different velocities in a dimensionless form as Froude (depth) numbers. The Froude depth number $F_{r,d}$ is the ratio between the velocity U and the maximum linear wave speed in shallow water C.

$$F_{r,d} \equiv \frac{U}{C}. \tag{2.3}$$

The maximum wave speed C follows from the simplified shallow water equations and can be written as:

$$C = \sqrt{g\frac{A_{flow}}{B_{f.s.}}} \approx \sqrt{gh}. \tag{2.4}$$

With A_{flow}, the cross sectional area of the flow [m^2] and
$B_{f.s.}$, the width of the free surface [m].

The ratio of the free surface width $B_{f.s.}$ and the cross sectional area of the flow A_{flow} is for a rectangular channel equal to the water depth h. For a free floating ship the free surface width is equal to the canal width since the vessel sinks in the water level depression it creates. If an object does not displace in the vertical, e.g. because it is mounted on a rail, the width of the free surface $B_{f.s.}$ is reduced and the maximum wave speed C is slightly larger. Nevertheless the maximum wave speed is calculated as $C = \sqrt{gh}$, since the increase in wave speed is below 10%.

The velocity of the hull is consequently expressed dimensionless as:

$$F_{r,d} = \frac{V_s}{\sqrt{gh}}. \tag{2.5}$$

With V_s, the velocity of the hull [m/s] and
h, the water depth [m].

The set of equations highly simplifies the flow condition beside the hull. In this schematisation the water level depression, z_a, and depth averaged return current, U_r, are uniform in lateral direction. To compensate for the non uniformity of the velocities a correction factor α_u is suggested in Jansen and Schijf (1953), since the average of the velocities squared is not equal to the square of the average velocities. The compensation factor α_u is empirically derived in Jansen and Schijf (1953) as:

$$\alpha_u = 1.4 - 0.4\frac{V_s}{\sqrt{gh}}. \tag{2.6}$$

The geometries of the canal and ship required for the calculation can made dimensionless by defining a factor K, representing the blockage:

$$K = \frac{A_s}{A_c}. \tag{2.7}$$

Identically the width of the free surface can be made to a dimensionless factor β:

$$\beta = \frac{B_{f.s.}}{B_c}. \tag{2.8}$$

Combining (2.1), (2.2), (2.7) and (2.8) a single fundamental equation of a ship moving through a canal can be derived, as shown in Lap (1954):

$$\frac{V_s}{\sqrt{gh}} = \frac{V_s + U_r}{\sqrt{gh}} \left\{ 1 - K - \frac{\alpha_u \beta}{2} \left(\left(\frac{V_s + U_r}{\sqrt{gh}} \right)^2 - \left(\frac{V_s}{\sqrt{gh}} \right)^2 \right) \right\}, \tag{2.9}$$

or dimensionless numbers:

$$F_{r,d} = F^*_{r,d} \left\{ 1 - K - \frac{\alpha_u \beta}{2} \left({F^*_{r,d}}^2 - {F_{r,d}}^2 \right) \right\}. \tag{2.10}$$

With $F_{r,d}$, the Froude depth number (ship speed relative to the bank) [-],
$F^*_{r,d}$, the Froude depth number relative to the return flow ($\frac{V_s+U_r}{\sqrt{gh}}$)[-],
K, the blockage factor [-],
α_u, the velocity distribution coefficient [-] and
β, the free surface width factor [-].

According to Lap (1954) the basic solution of fundamental equation (2.9) was first derived by Kreitner. For a free floating ship ($\beta = 1$) and assuming an uniform velocity distribution ($\alpha_u = 1$) Kreitner illustrated the results in one graph, figure 2.3.

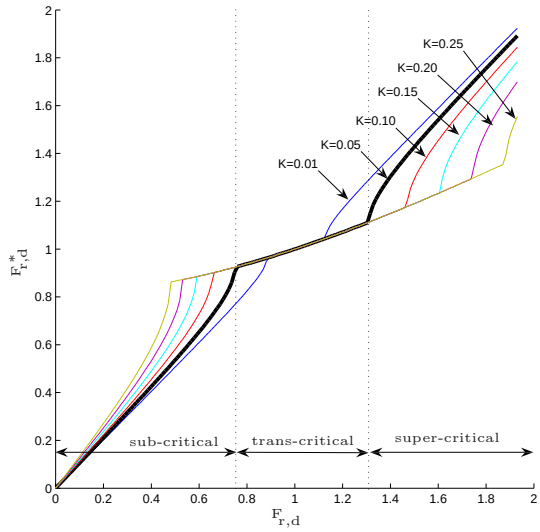

Figure 2.3: Relation between water speed alongside a ship in a canal and the ship speed relative to the bank for different, after Kreitner. The sub-critical, trans-critical and super-critical zones are indicated for K=0.05 (5 % hull area).

From Kreitner's graph the return current can be derived given a certain water depth h, blockage K and hull speed V_s. The water level set down is proportional to the velocity beside the hull squared, as can be seen from equation (2.2). The dimensionless set down $\frac{z_a}{h}$ is depicted for an arbitrary blockage in figure 2.4. In the super-critical domain the water level beside the hull lowers whereas in the sub-critical domain the water level beside the

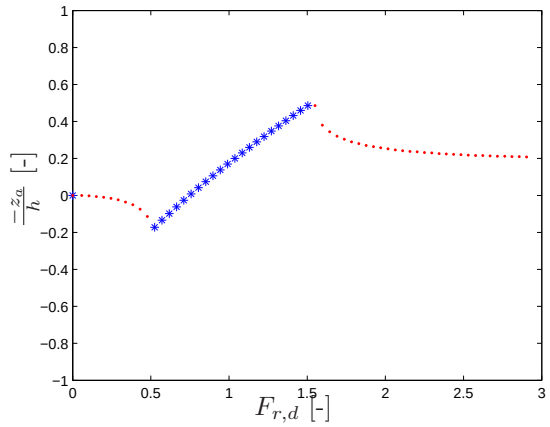

Figure 2.4: Setdown as function of the $F_{r,d}$ number for $K = 0.18$ (18 % Hull area).

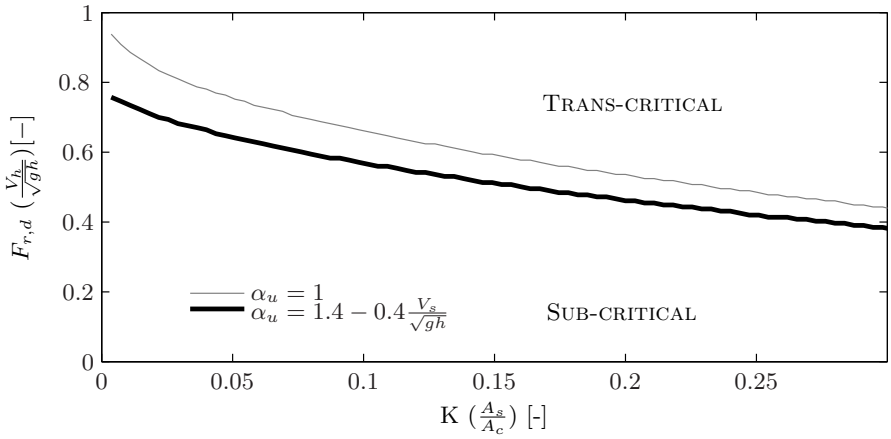

Figure 2.5: Boundary between sub-critical and trans-critical behavior.

hull is theoretically higher in order to comply equations (2.1) and (2.2). At the edges of the trans-critical domain the primary wave is theoretically at it largest.

For hull velocities close to $F_{r,d} = 1$ it is impossible to comply to both equations. Within this trans-critical range the cross-section beside the hull is too small for the discharge calculated with (2.1), given a certain energy head. The width of the trans-critical range depends on the blockage K as can be seen in figure 2.3. In case of a large vessel in a narrow channel, the blockage is high and the trans-critical domain starts at small Froude depth numbers. A vessel sailing in open water has theoretically no trans-critical range. The maximum velocity in the sub-critical range as function of the blockage K is depicted in 2.5.

The surplus of discharge is piled up before the hull and as a consequence a positive wave of translation preceding the hull and a smaller negative wave of translation behind the hull can be observed. This behavior is schematised in figure 2.6.
Dragging the hull within the trans-critical range will result in a time-dependent solution, where the translation wave will constantly be fed with water.

The surplus of discharge stored in the positive translation wave is:

$$\Delta Q = A_c V_s - (A_c - A_s - z_a(B_c - B_s))(V_s + U_r). \tag{2.11}$$

Where the discharge needed for a translation wave of height h_{t_+} above MWL can be calculated as follows:

$$\Delta Q = B_c h_{t_+} \sqrt{g(h + h_{t_+})}. \tag{2.12}$$

Combining (2.11) and (2.12), the height h_{t_+} can be calculated. The height of the translation wave grows as the hull is dragged closer to $F_{r,d} = 1$. Maximum height of the translation wave is bound to the depth induced breaking limit ($h_{t_+} \approx 0.5$ to $1.0\ h$).

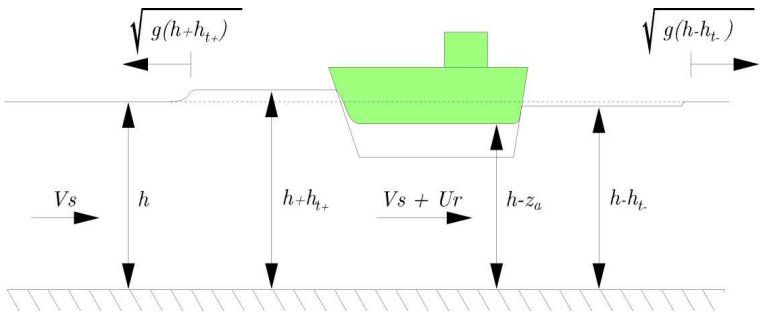

Figure 2.6: Trans-critical primary wave pattern.

Secondary wave

As mentioned in the introduction of this section, the secondary waves are a result of a moving disturbance point. An interference pattern is created behind the vessel, forming a typical V-pattern in deep water. The wave pattern is stationary with respect to the hull, which implies that the longitudinal velocity component of all waves must equal the hull velocity. The hull velocity v as used from hereon, is the velocity of the hull with respect to the water. Subsequently the following also holds for a fixed vessel in an opposing current with velocity v.

Figure 2.7: Deep water ship wave pattern. PHOTOGRAPH BY ADRIAN PINGSTONE.

The exact description of secondary wave pattern in deep water has been derived first by Lord Kelvin and is the subject of many publications (Stoker (1957)). In deep water (roughly when $F_{r,d} \leq 0.6$ as shown in the upcoming section) it has the same shape regardless of the speed or shape of the vessel. The V-pattern consists of diverging and transverse waves. These waves interfere on a line about 19 ° (θ) with the sailing line. The resulting interference cusps (called featherlet waves) lie on this interference line. The featherlet waves have an angle ϕ of about 55 ° with the sailing line. The full pattern with angles is derived in appendix A.1. The result is shown in figure 2.8.

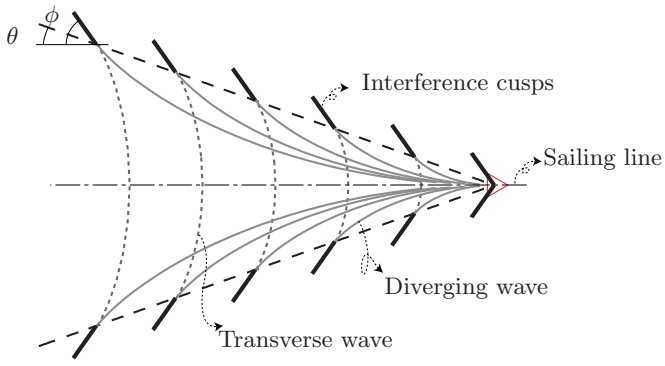

Figure 2.8: Deep water secondary wave pattern. Interference cups of the diverging and transverse waves lie on the interference line which encloses an angle θ of 19° with the sailing line. The angle of the featherlet waves ϕ is 55°.

In shallow water the interference angle and featherlet wave angle are larger, and increases up to 90°, which is derived graphically in appendix A.2 (see figure 2.9). When the ship travels very close to $F_{r,d} = 1$ a shock wave is formed, which can be compared to the sound barrier for flying objects.

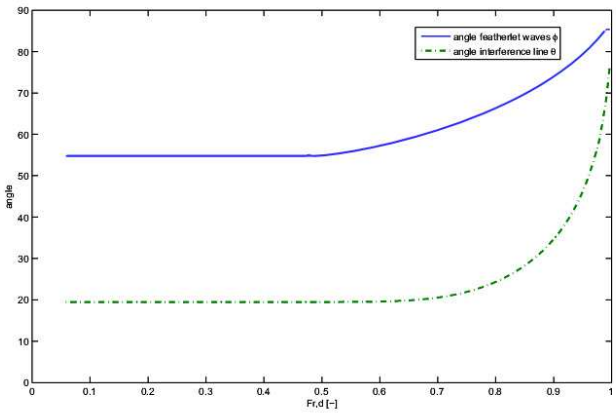

Figure 2.9: Computed wave angles as function of $F_{r,d}$.

The wave speed of the featherlet waves C then follows from the wave angle ϕ and the speed of hull with respect to the water v:

$$C = v \sin(\phi). \tag{2.13}$$

Free surface waves comply to the dispersion relation, which is derived and extensively treated upon in Stoker (1957). According to the dispersion relation, the wavelength L is dependent on the wave period T and water depth h.

$$L = \frac{gT^2}{2\pi} \tanh(\frac{2\pi h}{L}). \tag{2.14}$$

The wave period T is expressed in the wave length L and wave speed C using the identity:

$$T = \frac{L}{C}. \tag{2.15}$$

Hence, the wave length follows from substituting (2.15) and (2.13) into dispersion relation (2.14) and solving iteratively:

$$L = \frac{2\pi v^2 \sin^2(\phi)}{g} \frac{1}{\tanh(\frac{2\pi h}{L})}. \tag{2.16}$$

The transverse waves cross the sailing line at an angle $\phi = 0$. The tranverse wave length is hence:

$$L_t = \frac{2\pi v^2}{g} \frac{1}{\tanh(\frac{2\pi h}{L_t})}. \tag{2.17}$$

The deep and shallow water regimes follow from equations (2.16) and (2.17). For Froude depth numbers below 0.6 the water is considered deep, since the influence of the term $(\tanh(\frac{2\pi h}{L_t}))$ is smaller than 1 %, and the waterdepth h has therefore no significant influence on the wave pattern. This is confirmed by figure 2.9.

Wave heights The height of the interference cusps has been the subject of various research projects. None of these however resulted a sound theoretical relation between the hull shape and velocity versus the wave height. Several formulas are nevertheless derived for a small range of conditions based on experimental data. The work of several of these research projects is reviewed and summarized in Verheij and Bogaerts (1986). Generally speaking the observed wave height at location y from the ship is a function of the ships geometry, water depth h, velocity v and this distance to the ship y.

$$H = f(L_s, B_s, D_s, h, v, y). \tag{2.18}$$

The interference cusps as described in the previous paragraph can be described as a superposition of point disturbances. The strength of these point disturbances and consequently the interference cusps is related to the pressure gradients close to the hull. A sharp bow generates large pressure changes over a short length, and consequently large waves. The overall length of the vessel L_s is remarkably only of minor importance. The decay of the featherlet wave height in deep water is proportional to $y^{-1/3}$, which is mathematically derived in Havelock (1908). For speeds up to $F_{r,d} = 1$ this decay rate is confirmed by MCA (2001).

Equation (2.19) gives an indication for the cusp heights to be expected for deep water ship waves ($\theta = 19.47^\circ$).

$$H/h = \alpha_1 \left(\frac{y}{h}\right)^{-1/3} (F_{r,d})^{\alpha_2} . \tag{2.19}$$

With H, the wave height [m],
h, the waterdepth [m],
y, the distance to the bow perpendicular to the sailing line ($y > 0$) [m],
$F_{r,d}$, the Froude depth number $\frac{V_s}{\sqrt{gh}}$ [-],
α_1, shape coefficient [-] and
α_2, dimensionless waveheight :: Froude depth number coefficient [-].

The coefficient α_1 is associated with the geometry of the vessel. As mentioned previously the pressure gradients are localized around changes in cross section of the hull. Uniform parts amidships therefore barely contribute to the pattern and the overall length of the hull, L_s, has a small influence. The changes in the cross section can be characterized by D_s/L_e (with L_e, the entry length, the length from the bow to the parallel cross section). It can be computed for a specific hull shape but generally speaking the coefficient varies from 0.35 for (unloaded) slender ships to 1.0 for more blunt hull shapes. The relation between the waveheight and Froude depth number is given by the exponent α_2, and an $\alpha_2 = 4$ showed the best agreement with experimental data.

Figure 2.10 shows cusp height as function of the Froude depth number (based on a blunt hull shape, $\alpha_1 = 1.0$).

Large waves, in the order of the required 2 m, are only generated in deep basins when towing at a high velocity.

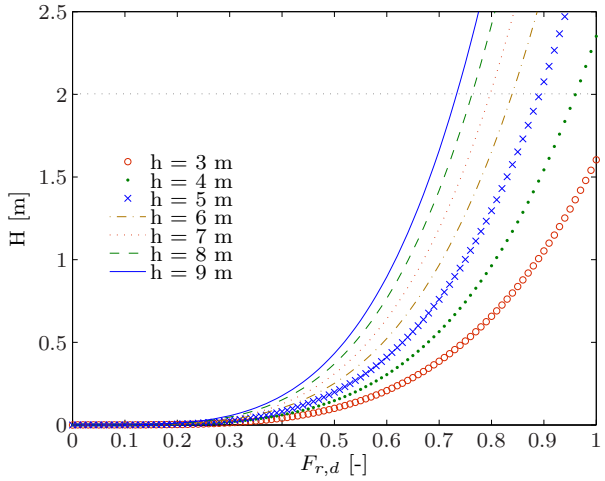

Figure 2.10: Wave heights at 20 m from the sailing line as function of $F_{r,d}$ according to Verheij and Bogaerts (1986). Note that waveheights in the region $F_{r,d} > 0.8$ are overestimated.

Unlike the primary wave, the secondary waves are free surface gravity waves. Under influence of a sloping topography these waves will break. The transformation of the secondary wave pattern generated close to the hull to a surf able breaker on the slope will be the subject of the upcoming sections.

2.2 Wave refraction

The waves generated by the vessel are free-surface gravity waves and propagate through the domain similar to wind waves found in the ocean. Their wave length L as well as wave celerity C decreases under influence of the water depth. This is called shoaling. Wave period however remains equal since the amount of wave crests in a fixed timespan has to remain the same. The period can be calculated using equation (2.15).
The local wavelength L on the slope at waterdepth h is given by the dispersion relation:

$$L = \frac{gT^2}{2\pi} \tanh(\frac{2\pi h}{L}), \tag{2.20}$$

and the wave speed C at waterdepth h:

$$C = \frac{gT}{2\pi} \tanh(\frac{2\pi h}{L}). \tag{2.21}$$

So, the wave speed decreases as waves travel up the slope. If the waves approach the slope under an angle ϕ, the waves crest will have to turn more and more shore parallel. This is called refraction and is illustrated in figure 2.11. The wave angle with respect to the cross shore direction Φ can be calculated by Snel's law:

$$\sin\Phi = \frac{C}{C_o} \sin(\Phi_o). \tag{2.22}$$

With Φ, the wave angle at the point of interest [-],
Φ_o, the wave angle near the hull [-],
C, the phase speed of the wave at the point of interest [m/s] and
C_o, the phase speed of the wave near the hull [m/s].

The wave angle and wave phase speed near the hull are a result of the calculated wave pattern as decribed in the last section. Using the identities $\Phi_o = \phi$ and $C_o = V_h \sin(\phi)$ equation 2.22 reduces to:

$$\Phi = \sin^{-1}\left(\frac{C}{V_h \sin(\phi)} \sin(\phi)\right) = \sin^{-1}\left(\frac{C}{V_h}\right). \tag{2.23}$$

The amplitude of the waves changes due to the shoaling and refraction. Wave energy is redistributed along the wave crest by refraction which reduces the wave height, whereas the shoaling increases the wave height. The influence of both can be included using:

$$H = H_o K_r K_s. \tag{2.24}$$

With H_o, the wave height at deep water [m],
K_r, the refraction factor [-] and
K_s, the shoaling factor [-].

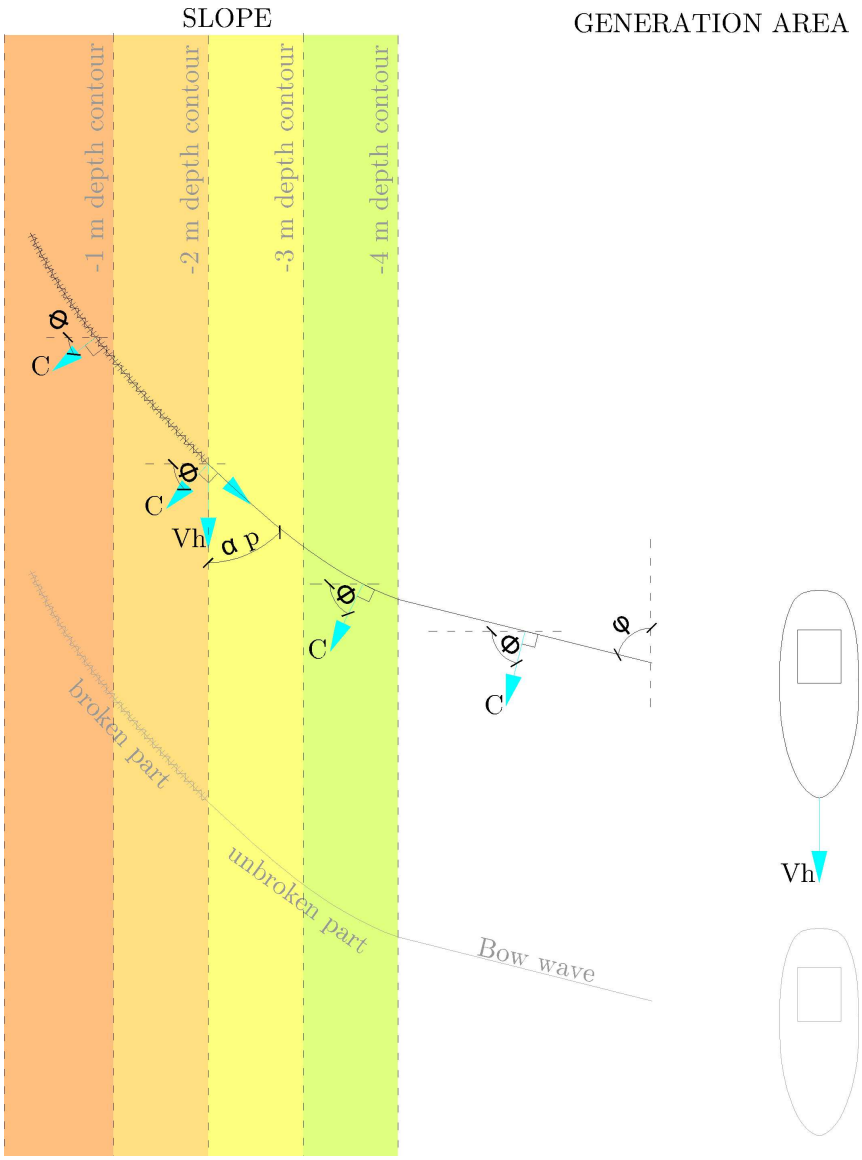

Figure 2.11: Refraction in a straight channel.

For slowly varying depths both factors K_r and K_s follow from wave energy conservation. Mei (1989) derives the following refraction and shoaling factors:

$$K_r = \sqrt{\frac{\cos(\Phi_0)}{\cos(\Phi)}}, \tag{2.25}$$

and

$$K_s = \sqrt{\frac{C_{go}}{C_g}} = \sqrt{\frac{n_o C_o}{nC}}. \tag{2.26}$$

With C_{go}, the group velocity of the waves near the hull [m/s],
C_g, the group velocity of the waves at the point of interest [m/s],
n_o, the ratio between group and phase velocity near the hull [-] and
n, the ratio between group and phase velocity at the point of interest [-].

Where the ratio between group and phase velocity is given by:

$$\frac{Cg}{C} \equiv n = \frac{1}{2} + \frac{\frac{2\pi h}{L}}{sinh(\frac{4\pi h}{L})}. \tag{2.27}$$

According Dally (2001) waveheight in very shallow water is underestimated by linear theory. The very shallow water region defined in Dally (2001) is given by $h < \sqrt{\frac{gHT^2}{30}}$. He cites an alternative (non linear) shoaling factor (based on cnoidal theory) proposed by Shuto for the very shallow water range up to breakpoint:

$$K_s = \sqrt{\frac{h^{4/7}}{h_b^{4/7}}}. \tag{2.28}$$

The wave height is calculated using (2.24), using a shoaling factor K_s calculated with (2.26) up to the very shallow water limit, and K_s calculated with (2.28) thereafter.

2.3 Wave breaking on a slope

As waves propagate onto a slope their shape changes. Under influence of the decreasing water depth the troughs flatten and crests sharpen until finally the wave breaks. This is called shoaling. The breaker shape as well as the water depth under a breaking wave are given by Battjes (1974) of which the relevant conclusions will be recited and reformulated hereunder.

Water depth at breakpoint The water depth under a breaking wave is determined using the factor γ:

$$h_b = \frac{H_b}{\gamma}. \tag{2.29}$$

With H_b, the wave height height at breakpoint [m],

h_b, the waterdepth height at breakpoint [m] and
γ, breaker depth coefficient [-].

The coefficient γ is dependent on the the type of wave breaking. For regular plunging waves, γ has proven to be about one.

$$h_b \approx H_b. \tag{2.30}$$

Hence, the breakpoint of a 2 m wave will be around the 2 m depth contour.

Breaker type The wave can break in different breaker shapes, of which the spilling and plunging types are the most important. Whether the first or latter occurs depends on the relative steepness of the slope in relation to the steepness of the wave. This ratio is captured in the surf similarity or Iribarren parameter:

$$\xi = \frac{\tan\alpha}{\sqrt{H/L_o}}. \tag{2.31}$$

With α, the steepness of the slope [-],
L_o, the wavelength [m] on deep water and
H, the wave height at breakpoint [m].

The Iribarren parameter as derived in Battjes (1974) assumes a wave propagating from deep water with wave length L_0 and breaking in shallow water. In case of short ship waves ($L = O(10m)$) in a shallow pool ($h = O(3m)$) this is an inconvenient way to compare the since the waves are not generated in deep water and break in water of intermediate depth.

The wavelength on deep water is given by:

$$L_o = C_{deep}T = \frac{gT^2}{2\pi}, \tag{2.32}$$

and for shallow water the following holds:

$$L_b = C_{shallow}T = \sqrt{gh_b}T. \tag{2.33}$$

Elimination of T between (2.32) and (2.33) gives a relation between the wavelength on deep water and at breakpoint:

$$L_o = \frac{L_b^2}{2\pi h_b}. \tag{2.34}$$

So (2.31) is reformulated using (2.34) into an expression only dependent on values at breakpoint:

$$\xi = \frac{\tan\alpha}{\sqrt{2\pi\frac{H_b h_b}{L_b^2}}}. \tag{2.35}$$

Waterdepth h_b under a breaking wave is about equal to the waveheight H_b as stated in the last section. The Iribarren parameter can therefore be simplified to the ratio between the slope of the bottom and the steepness of the wave at breakpoint:

$$\xi = \frac{\tan\alpha}{\sqrt{2\pi H_b/L_b}}. \tag{2.36}$$

The experimental values of ξ as used commonly and described by Battjes (1974) are listed in table 2.1. The values based on a plane slope with wave crests parallel to the depth contours. These values of ξ have proven to be accurate for non-uniform slopes with oblique waves as well (Henriquez (2004)). In this case the steepness of the slope has to be taken perpendicular to the wave crest:

$$\xi = \frac{\tan\alpha \ \cos\Phi_b}{\sqrt{2\pi}H_b/L_b}. \tag{2.37}$$

With α, the steepness of the slope in cross shore direction [-],
Φ_b, the wave angle at breakpoint [-],
L_b, the wavelength at breakpoint [m] and
H_b, the wave height at breakpoint [m].

Table 2.1: Iribarren parameter values

Breaker type	Value ξ
spilling	ξ<0.4
plunging	0.4<ξ<2.0
surging/collapsing	ξ>2.0

3
Physical model study

3.1 Introduction

The flow behind and around the hull as described in chapter 2 is verified by experiments in a towing tank. Although described separately in the last chapter, primary and secondary wave system are interrelated. The influence of the water level depression and return flow beside the hull (primary wave) on the generation of the secondary wave field is determined in this experiment.
The objective of these experiments is to map the resemblances and differences of the combined primary and secondary wave theory with a physical experiment as well as producing a dataset to validate future numerical modeling.

In order to achieve these objectives an experiment organized, towing hulls with different cross sectional area in a towing tank at the Ship Hydromechanics Laboratory of the faculty of Mechanical, Maritime and Materials Engineering (Delft University of Technology). A physical model is designed on a $1:10$ scale, based on the maximum towing velocity of the facility.
Three different hulls are fabricated, having a length of 1.3 m but varying in beam B, specified in appendix B. The hulls are towed in a towing tank while varying the towing velocity V_{tow} and draft D (see table 3.1).

The generated wave field is captured using in situ instruments measuring the surface elevation and velocity. Furthermore the wave field is photographed with a two cameras, a stereo photogrammetry setup [1] (see figure 3.1). Throughout the experiments the water motion is recorded, which is used in the analysis to determine whether waves were breaking and flow was detaching.

According to Stive (1985) scale effects on wave height (and wave induced velocities) in the range 0.1m to 1.5m are negligible. The generated wave heights thus can be scaled geometrically with the $1:10$ length scale. Velocities scale by the Froude velocity scale, the square root of the length scale, $1:\sqrt{10} \approx 1:3.2$.

[1] The stereo photogrammetry will not be elaborated here, the reader is referred to de Vries (2007)

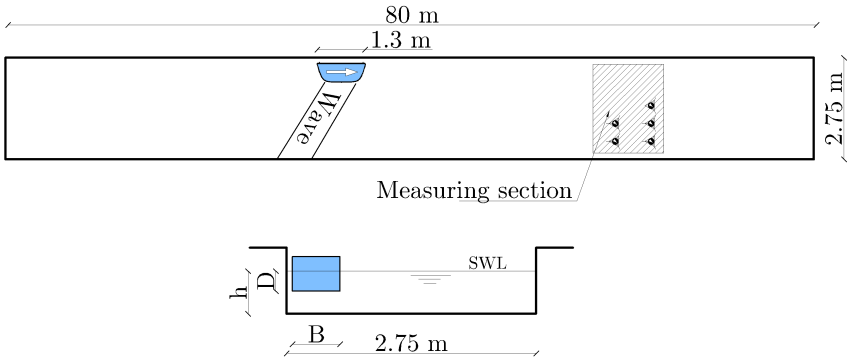

Figure 3.1: Experiment setup, topview and cross-section.

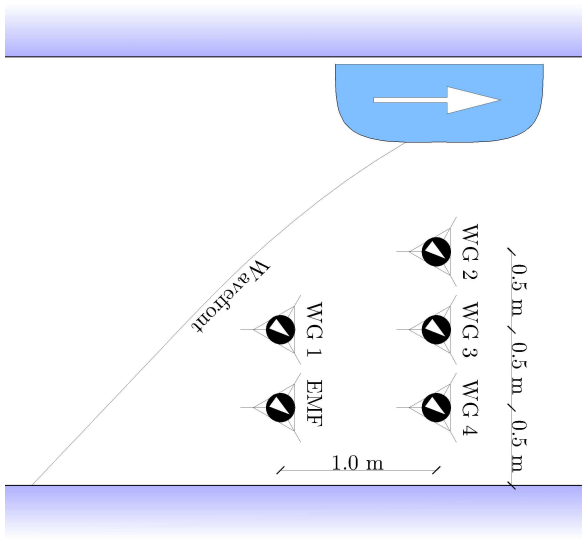

Figure 3.2: Measuring section.

Towing tank facilities are intended for towing small objects. Towing these relatively large hulls has some drawbacks. The computer controlled carriage towing the hull is incapable to tow objects with large blockage at high speeds due to the limited traction of the wheels and length of the tank. The largest hull can therefore not be towed close $F_{r,d} = 1$.
Furthermore measured velocity V_h deviates from the input velocity V_{tow}(the velocity as entered on the control panel) especially when a large object is towed and a large force is exerted on the carriage.

The generated waves are captured by measuring devices which are positioned in an array (see figure 3.2). Using four wave gauges in a triangular array provides information on the surface elevation in time and space.
The ensemble of WG 2, WG 3 and WG 4 positioned in lateral direction are intended to provide information on the lateral change in water level depression z_a. The surface elevation time series of WG 1 and WG 3 provide information on the speed of the hull and the stationarity of the wave field.

The velocities are measured with an electro-magnetic field meter (EMF), positioned 500 mm from the tank wall and 100 mm from the bottom of the tank. All instruments are sampled at 100 Hz.

Table 3.1: Experiments

Test type	waterdepth h [m]	draft D [m]	hull type B	input velocity V_{tow} [m/s]	$F_{r,d}$ based on the input velocity ($\frac{V_{tow}}{\sqrt{gh}}$) -
T1.1 Statistic	0.51	0.49	Hull type 1	0.7(5x)	0.31(5x)
T1.2	0.51	0.49	$B = 0.5m$	1.4(5x)	0.63(5x)
T2.1 Waterdepth	0.41	0.39		1.26(2x), 1.64	0.63(2x), 0.82
T2.2	0.32	0.30		1.12(2x), 1.87, 1.95	0.63(2x), 1.06, 1.10
T2.3	0.25	0.23		0.99(2x), 2.10	0.63(2x), 1.34
T3.1 Medium beam	0.31	0.29		0.6(2x), 0.8(2x), 1.0, ...1.2, 1.4, 1.6, 1.8	0.34(2x), 0.46(2x), 0.57, ...0.69, 0.80, 0.92, 1.03
T3.2	0.31	0.19		0.6, 1.0, 1.4, 1.8	0.34, 0.57, 0.80, 1.03
T3.3	0.31	0.09		0.6, 1.0, 1.2, ...1.4, 1.8, 2.3	0.34, 0.57, 0.69, ...0.80, 1.03, 1.32
T4.1 Large beam	0.31	0.29	Hull type 2	0.6, 0.8, 1.0, 1.2, 1.4	0.34, 0.46, 0.57, 0.69, 0.80
T4.2	0.31	0.19	$B = 0.83m$	0.6, 0.8, 1.0, 1.2, 1.4	0.34, 0.46, 0.57, 0.69, 0.80
T4.3	0.31	0.11		0.6, 0.8, 1.0, 1.2, 1.4	0.34, 0.46, 0.57, 0.69, 0.80
T5.1 Narrow beam	0.30	0.28	Hull type 3 $B = 0.37m$	0.6, 0.8, 1.0, ...1.2, 1.4, 1.8	0.35, 0.47, 0.58, ...0.70, 0.82, 1.05
T5.2	0.30	0.19		0.6, 0.8, 1.0, 1.2, ...1.4, 1.8, 2.0, 2.3	0.35, 0.47, 0.58, 0.70 ...0.82, 1.05, 1.17, 1.34
T5.3	0.30	0.09		0.6, 0.8, 1.0, 1.2, ...1.4, 1.6, 1.8, 2.0	0.35, 0.47, 0.58, 0.70 ...0.82, 0.93, 1.05, 1.17

3.2 Observations

A wide variety of flow patterns is observed during the experiments, depending on the hull shape and velocity. Two extremes are used to clarified hereunder.
First, a run with small blockage and hull velocity. The return current is only a fraction of the hull velocity, since the flow is only slightly contracted. The return flow is concentrated close to the hull, and so is the water level depression. The secondary wave pattern constructed behind the hull is barely influenced by the primary wave pattern and has a perfect V-pattern.

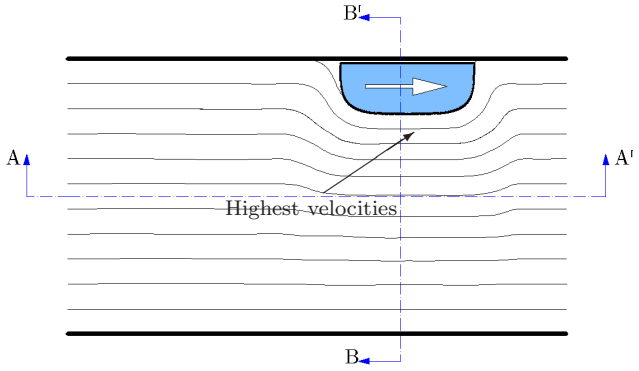

Figure 3.3: Top view, primary wave flow around a narrow hull towed at small velocity.

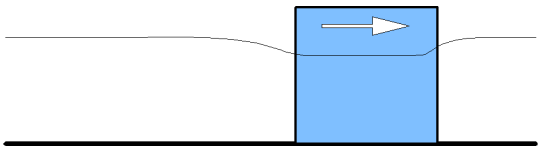

Figure 3.4: Longitudinal cross section AA', primary wave.

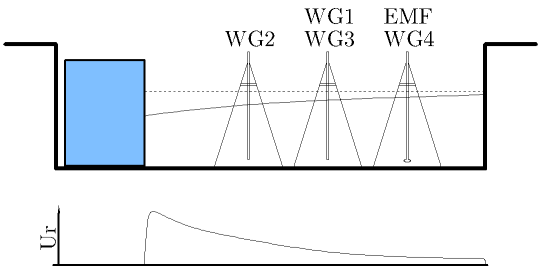

Figure 3.5: Lateral cross section BB', water level and velocity distribution primary wave.

The other extremity is a run with a large velocity and blockage. A translation wave is generated before the hull, since the cross section beside the hull is too small for the discharge (As elaborated in chapter 2). The flow detaches near the front of the hull and is highly contracted. The effective cross section for the flow is hence reduced even further. Velocities increase beside the hull beyond $F_{r,d} = 1$ and a curved hydraulic jump is formed. The secondary wave field is constructed in this non uniform flow field and is hardly visible.

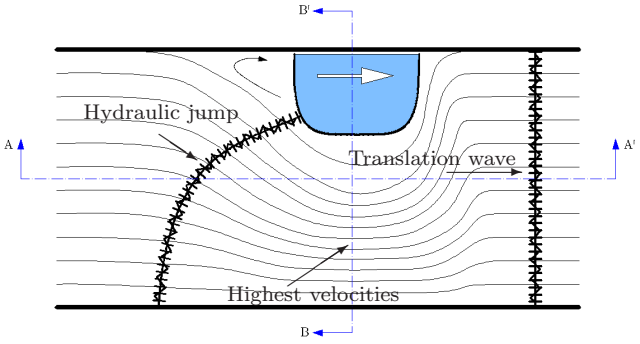

Figure 3.6: Top view, primary wave flow around a wide hull towed at large velocity.

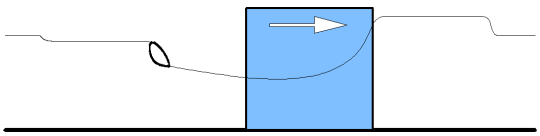

Figure 3.7: Longitudinal cross section AA', primary wave.

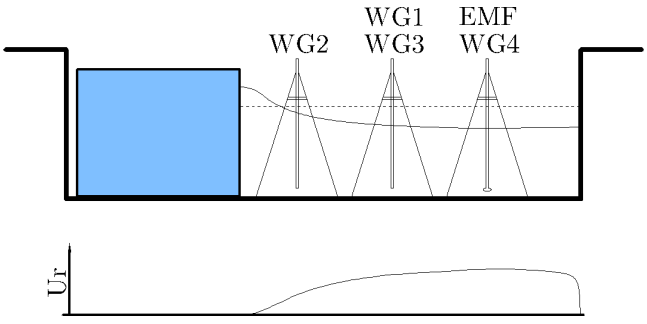

Figure 3.8: Lateral cross section BB', water level and velocity distribution primary wave.

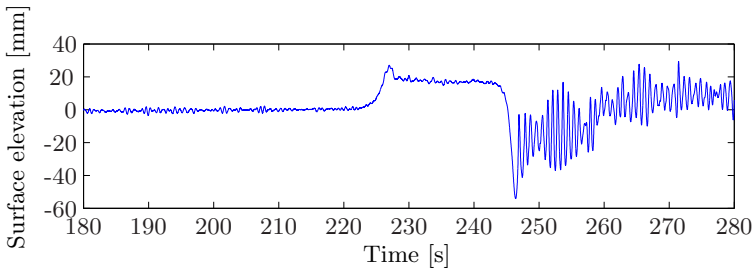

Figure 3.9: Raw wave gauge signal T4.2 1.0 m/s. Hull passes the wave gauge around t=245 s preceded by a translation wave. Lowest water level in the time domain is the local water level depression,(z_a), near the hull. The secondary wave is visible after this depression.

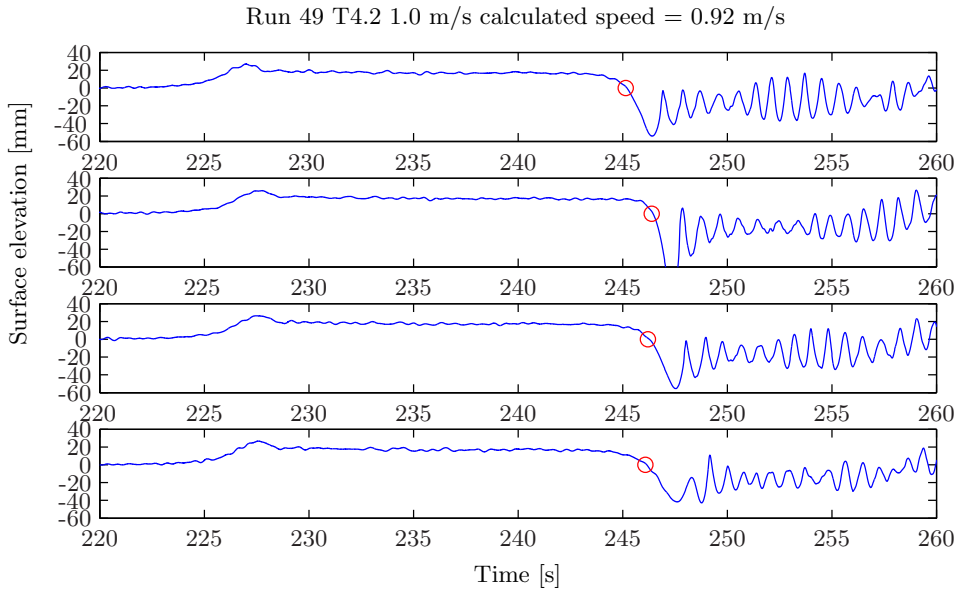

Figure 3.10: Main zero crossings marked as '**o**' for WG 1,WG 2, WG 3 and WG 4 *(from top to bottom).*

3.3 Method

Raw time series obtained from the wavegauges typically resemble the signal depicted in figure 3.9. In the first part of the time series only small ripples are visible. These ripples are left over from previous test and are a few mm high with a period smaller than a second. Next the translation wave passes the wavegauge. The translation wave precedes the hull and the front of this shock wave occasionally has some oscillations on top. Then the hull passes the wave gauges and the water level lowers, the local water level depression (z_a) is generally the lowest water level in the time domain. The secondary wave is visible after this depression.

The surface elevation is a result of different processes. To compare the different runs the signal is sifted (separated) into a primary and secondary wave part. Main features of both parts can be described by a small number of typical features. The primary wave can be schematised by a water level depression z_a and return current U_r beside the hull. Secondary wave field is characterized by a wave height H and period. These can be extracted by consequently:

- Denoising the data
- Locating the hull passage
- Sifting the primary and secondary wave from the signal

Denoising

The signal obtained from the resistance-type wave gauges contains a small amount of noise which leads to several local maxima and minima in the signal within 0.5 s. These small riding waves will make it difficult to distinguish the secondary waves as minima and maxima in the signal later on. Since the noise has no physical meaning, the raw signal from the gauges is filtered using a linear filter, averaging over 0.1 s. The averaging period is selected roughly an order of magnitude smaller than the wave period to minimize the influence of the averaging on the wave height.

Locating the hull passage in the time series

Locating the passage of the hull is essential for the comparison of individual runs as well as separating the secondary wave behind the hull from the rest of the signal. The passage of the hull is characterized by a water level depression (z_a) preceded by a translation wave for runs in the trans-critical region. A main zero crossing is defined as the down crossing of the primary wave near the hull. Figure 3.10 shows the locations of the main zero crossings for all wave gauges.

As expected, the time of this main zero crossing differs for all wave gauges, since hull passes WG 1 before WG 2, 3 and 4. The difference between time of the zero crossing for WG 1, T_{WG1} and WG 3, T_{WG3} is used to calculate the speed of the hull.

$$V_h = \frac{1.0m}{T_{WG3} - T_{WG1}}. \tag{3.1}$$

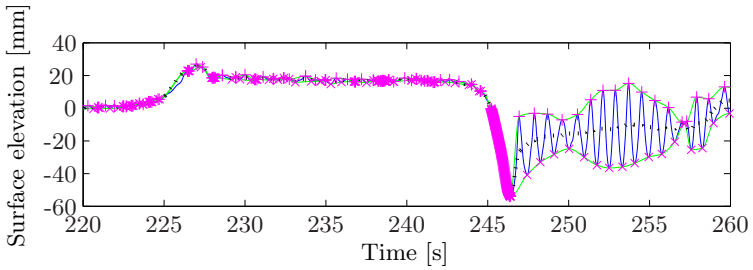

Figure 3.11: Envelopes T4.2 1.0 m/s. Local maxima (+) and minima (x) interpolated with a cubic spline to produce envelopes of the signal.

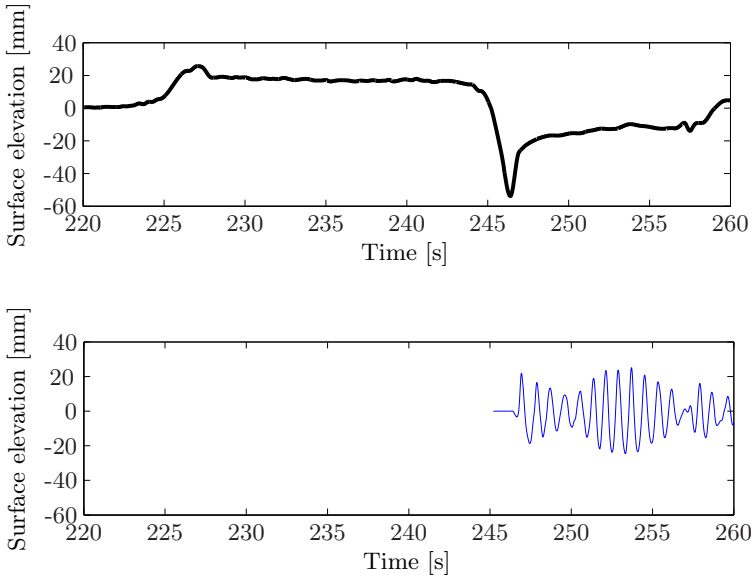

Figure 3.12: Primary wave (*top*) and secondary wave T4.2 1.0 m/s. Two modes sifted from figure 3.11.

Sifting

The signal consists of the primary wave system and the secondary wave system imposed on each other. For better understanding these two 'intrinsic modes' are analyzed separately. The two modes in the signal can be separated by looking at different timescales of the two modes, just as the human eye would do.
The difference in timescales is visible in the local maxima and minima. The primary wave has mostly features with timescales in the order of multiple seconds, whereas the secondary wave period is about a second.
Common procedure to sift to two modes with different timescales is high or low-pass frequency filtering. Frequency filtering is however doubtful, since the waterlevel depression, z_a, beside the hull has about the same time scale as the secondary wave and will be falsely assigned to the secondary wave field.
Therefore the signal is sifted into two modes by an approach based on Emipirical Mode Decompostition (EMD) as described in Huang et al. (1996). The EMD procedure consists of mapping the local maxima and minima of the signal and then constructing two envelopes by interpolating these extrema (figure 3.11). The average of these envelopes is assumed to be an intrinsic mode in the signal, corresponding to the primary wave. Once revealed the primary wave can be subtracted from the original signal. The residue is the secondary wave (see figure 3.12).

> Note: The usual EMD procedure as presented by Huang beholds an iteration process where envelopes of a mode are recalculated until the standard deviation of the difference between consecutive means is below a threshold. This usually guarantees that the resulting modes have a physical meaning. The EMD procedure has nevertheless the same disadvantage as frequency filtering when the water level depression z_a is concerned. When modes have pronounced non-stationary features, each consecutive step of the iteration process smoothens the sharp edges, so with each step the residue moves further away from the physical meaning sought after.
> Consequently, in order to have these sharp features represented in the modes, this condition and corresponding iteration process are excluded. Furthermore, the procedure is modified using the a priori knowledge that the secondary wave train only occurs behind the hull, pinning the envelopes to the signal close to the main zero crossing (figure 3.11).

The primary and secondary wave signal as sifted from the original signal is simplified to a few variables. Comparison between different runs and theory is done using these variables. The primary wave system is reduced to the following variables:

- The maximum water level depression z_a and return current U_r near the hull passage.
- The average height h_{t_+} and the mean velocity U_{t_+} in the positive translation wave.

The secondary wave field is reduced to the following variables:

- The maximum wave height H.
- The wave period T.
- The wave angle Φ.

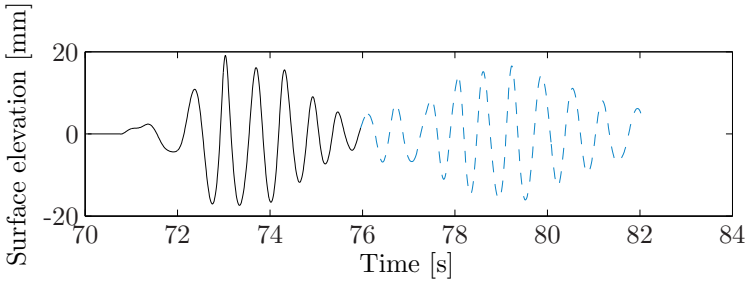

Figure 3.13: The measured secondary wave field. Unreflected (*solid line*) and reflected (*dashed*) from the tank wall. T3.2 1.0 m/s.

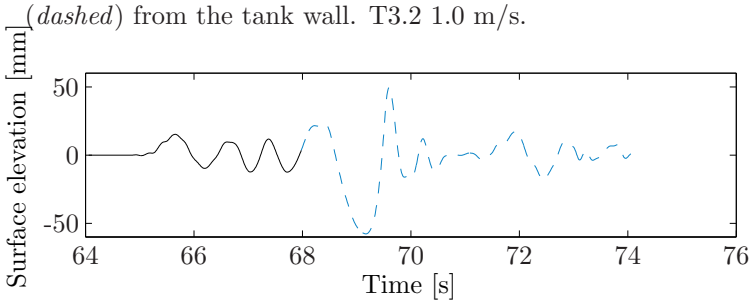

Figure 3.14: The measured secondary wave field. Unreflected (*solid line*) and reflected (*dashed*) from the tank wall. T4.1 1.4 m/s (The original signal is depicted in figure 3.16).

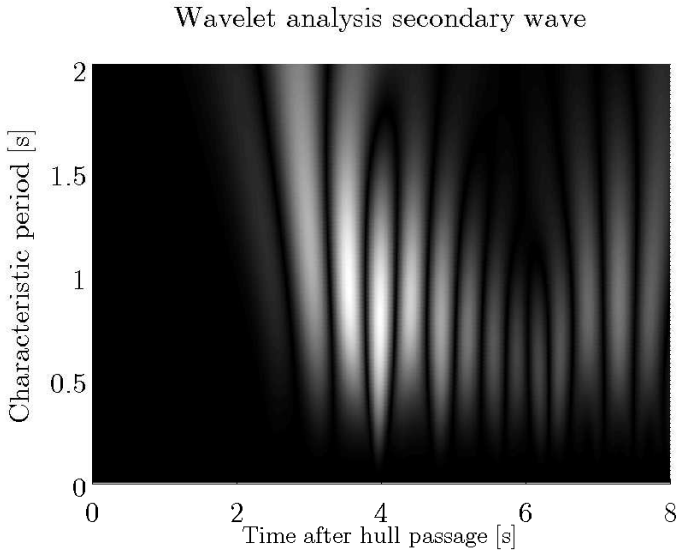

Figure 3.15: Scaleogram T4.2 1.0 m/s, lighter colors indicate high correlation. Secondary wave field as analysed in the CWT procedure is depicted in figure 3.12.

The secondary waves are the interference cusps behind the hull. The **maximum wave height** is defined as the largest interference cusp (difference between a local minimum and local maximum) before the wave field is reflected from the tank wall. In a measurement this appears as a wave group with the largest interference cusp in the middle, followed by the reflected signal. The boundary between reflected and unreflected waves is mostly determined from the camera recordings. When the hull is moving slowly the interference cusps theoretically lie on a line of 19.5 ° with the sailing line. Wave lengths are small and consequently the wave train consists of several unreflected waves (see figure 3.13). Faster runs have a larger wave angle ϕ and wave length. This implies that the waves are closer to the hull and its primary wave pattern and the number of unreflected waves is smaller. The wave pattern thus looks more chaotic (see figure 3.14).
The wave **period** is analyzed using a Continuous Wavelet Transform (CWT). The perceived period of the waves is not stationary, due to the return currents. The generated wave field depends on the velocity of the hull with respect to the water so a large return current influences the wavelength. A secondary wave field moving through a inhomogeneous velocity field has hence a time dependent period. Due to this time dependency an ordinary Fast Fourier Transform (FFT) cannot be used to analyze the period. Windowing the FFT like with an windowed Fourier analysis (WFA), is problematic due to the speed at which the return velocity changes. The window size is an arbitrary value, for it should be chosen long enough to capture the lower frequencies in the signal while at the same time guarantee stationarity of the data in the window. The return velocity changes considerably within one wave period so it is impossible to comply both demands. The timescales of the secondary wave field (the wave period) are therefore analyzed using a Continuous Wavelet Transform. Pseudo wave periods are determined locally, and the increase in wave period in areas with return current is represented correctly.

The CWT procedure captures the different timescales within the signal using a wavelet with a finite length. The procedure is as follows: A wavelet is shifted across the signal. At each time location the correlation **C** between the signal and the wavelet is calculated. Locations with high C values the wavelet form have a high resemblance with the signal. Once the whole signal has been evaluated the wavelet is scaled a step larger and compared to the signal once again. When shifting the wavelet in all sizes over the whole signal, structures of all time scales can be captured. The correlation **C** is calculated for each location in time and wavelet scale, as explained above. This can be visualized in a scaleogram (see figure 3.15). Wave crests and troughs are found in the scaleogram as locations with high correlation. The x axis is the time axis of the signal; the y axis is the scale a of the wavelet and the colors represent the correlation **C**. The scale of the wavelet can be converted to pseudo periods by $T = 1/4a$.

For an example and mathematical description of the wavelet procedure the reader is referred to appendix C.

Secondary **wave angle** can be computed out of the change in wave height between WG 2, WG3 and WG 4. Tracking down the same wave in the three gauge signals is not obvious and drawing conclusions based on three points is unreliable, especially when the wavecrest is curved. The angle of the wave crest is therefore retrieved from the stereo photogrammetry reconstruction of the water surface, described in de Vries (2007).

The variables z_a, U_r, h_{t_+}, U_{t_+}, H and T are extracted from the measuring devices with the methods mentioned for each run. Runs are compared with each other and theory in section 3.4.

3.4 Results

Reproducibility

Prior to drawing conclusions it is important to assess whether similar runs would give similar outcomes. Two tests, T1.1 and T1.2, are used to evaluate the significance and deviation of the experimental outcomes. Each test consists of 5 runs with nearly equal conditions. The desired hull velocity V_{tow} is set via the control panel, as 0.7 (T1.1) and 1,4 m/s (T1.2).
Unfortunately the velocity control on the towing carriage is inexact, consequently the actual hull velocity V_h (equation (3.1), page 29) is slightly slower and velocities of around 0.6 (T1.1) and 1.25 m/s (T1.2) are deducted from the surface elevation time series.
These measured velocities are found to deviate about 5 percent, not only because of the inexact velocity control of the carriage but also because of inaccuracies deducting this velocity. The velocity is deducted from the surface elevation time series by comparing the location of the main zero crossing (the zero crossing as the the hull passes). The determination of this main zero crossing is not evident, especially when ripples left over from the previous tests are only one order of magnitude smaller than the actual waves, as with low velocity runs.
The variation in velocity V_h makes it difficult to capture whether an equal run would provide equal results in terms of wave height H, water level depression z_a and return current U_r. Comparing the variation in the forcing (V_h) and the variation in the response (H, z_a and U_r) can however give insight on the reproducibility.
The variation in an arbitrary variable x is often expressed in a variation coefficient β, being the ratio of the standard deviation σ and the mean value $\bar{x}$. For a random variable x these follow from:

$$\sigma = \sqrt{\frac{1}{N}\sum_{i=1}^{N}(x_i - \bar{x})^2}, \tag{3.2}$$

where N represents the sample size, and the mean, $\bar{x}$, is calculated as follows:

$$\bar{x} = \frac{1}{N}\sum_{i=1}^{N} x_i. \tag{3.3}$$

The variation of the velocity V_h, wave height H, water level depression z_a and return current U_r are listed for the two tests in table 3.2.
For the first test, T1.1, the hull is towed at a small velocity, 0.61 m/s, corresponding to $F_{r,d} = 0.27$. For such slow runs the variation in velocity β_{V_h} is mainly caused by the inaccuracy in the velocity determination, instead of the actual velocity. The small variation in the return current and water level depression confirms this conclusion.
For the second test, T1.2, the hull is dragged at a larger velocity, 1.27 m/s, corresponding to $F_{r,d} = 0.57$. The main zero crossing can be clearly defined in the surface elevation time series, and the variability in the measured velocity can be fully attributed to the towing carriage. A large translation wave is formed before the hull, exerting a large force on the carriage and the velocity fluctuates slightly.
The variation in wave height is quite large $\beta_H = 0.11$ and is explained by looking at the corresponding velocities of the runs. Higher velocities simply generate higher waves, and

since the relation between hull velocity and wave height is of the fourth order (Verheij and Bogaerts (1986)), the variation β_H is larger than β_{V_h}.
It cannot be proven with this dataset, that two similar runs would give similar outcomes, at the utmost it can be assumed from table 3.2 that the deviation is sufficiently small. The statistical dataset however proves that the input velocity is not accurate. Further analysis is therefore done with the velocity deducted form the surface elevation time series, despite the inaccuracy of the method for runs with small waves.

Table 3.2: Statistical values of the reproducibility test

T1.1 Statistic input velocity 0.70 m/s	measured velocity V_h	values [m/s] 0.56 0.60 0.67 0.65 0.59	mean [m/s] 0.61	σ [m/s] 0.04	β [-] 0.06
	secondary wave height H	values [mm] 11 13 11 12 14	mean [mm] 12.4	σ [mm] 1.02	β [-] 0.08
	water level depression z_a	values [mm] 13 14 14 14 13	mean [mm] 13.6	σ [mm] 0.49	β [-] 0.04
	return current U_r	values [m/s] 0.18 0.18 0.17 0.18 0.18	mean [m/s] 0.18	σ [m/s] 0.004	β [-] 0.02
T1.2 Statistic input velocity 1.40 m/s	measured velocity V_h	values [m/s] 1.25 1.27 1.23 1.30 1.32	mean [m/s] 1.27	σ [m/s] 0.03	β [-] 0.03
	secondary wave height* H	values [mm] 75 75 75 95 91	mean [mm] 82	σ [mm] 8.9	β [-] 0.11
	water level depression z_a	values [mm] 183 179 171 196 201	mean [mm] 186	σ [mm] 11.0	β [-] 0.06
	return current U_r	values [m/s] 1.10 1.02 0.95 1.14 1.16	mean [m/s] 1.07	σ [m/s] 0.08	β [-] 0.07

**breaking*

Stationarity

Throughout this report the induced flow pattern is assumed to be stationary with respect to the hull. In that case the signals from WG1 and WG3 (which are standing 1 m behind each other) are similar, just shifted in time. The signal of WG1 is then equal to the signal of WG3 shifted by $\Delta t = \frac{1m}{V_h}$. These signals, WG1 and the shifted WG3, are shown in figure 3.16.
The run used for the first comparison, T4.1 1.4 m/s, is a run with high blockage and velocity, consequently a large translation wave and interference cusps are generated.
Comparing both signals the following can be noticed:
The water level set down z_a ($t \approx 3$ s) is identical in both signals. The translation wave before the hull is elongated, as can be expected since it is constantly fed with water in the trans-critical domain.
The first three waves ($3 < t < 6$ s) are the unreflected secondary wave field, the featherlet waves are about 30 mm high. The 4^{th} wave is a superposition of the 4^{th} featherlet wave with the reflection of the 1^{st}, the wave is therefore slightly larger.
At $t \approx 7.5$ s a hydraulic jump passes the wavegauge. The air in the hydraulic jump makes it impossible for the resistance type wave gauges to capture the water level precisely and a large difference between both signals is the result.
Finally, the positive translation wave (in front of the hull) reflects from the bottom end of the towing tank and returns as a turbulent bore. It can be seen around $t = 20$ s.

For a slower run with less blockage both signals are even more similar. Figure 3.17 depicts the signals for the run T5.2 1.2 m/s. The only difference between both signals are the small ripples left over from the preceding run (O(2mm)).
So, in summary, the wave pattern is found to be indeed stationary with respect to the hull.

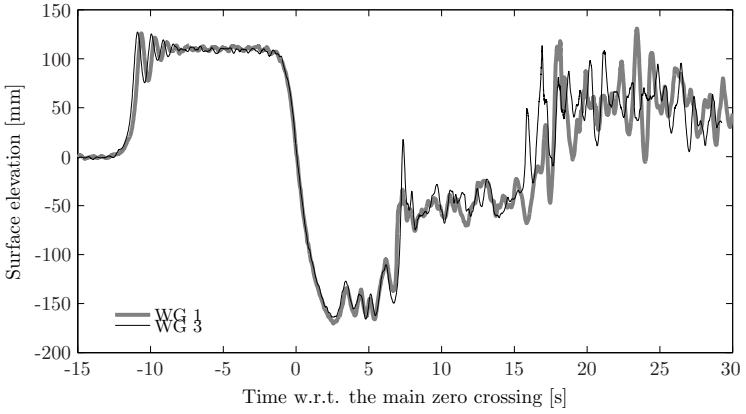

Figure 3.16: Comparison stationarity wave gauge signals WG 1 and shifted WG 3 (T4.1 1.4 m/s).

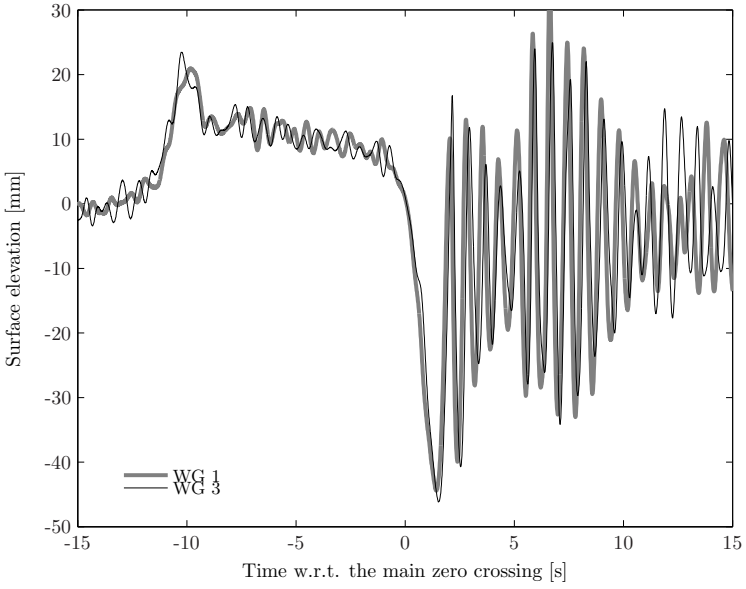

Figure 3.17: Comparison stationarity wave gauge signals WG 1 and shifted WG 3 (T5.2 1.2 m/s).

Primary wave pattern

The primary wave pattern concerns the flow near the hull. The water level beside the hull is lowered due to the increase in velocity, as elaborated in chapter 2. This lowering of the water table z_a and the increase of velocity U_r are measured to validate theory with the experiments. When the hull velocity is large, the cross section is not sufficiently large to discharge the water pushed alongside the hull and a translation wave is formed in front of the hull. This domain is called the trans-critical range, as mentioned before. The height of this translation wave h_{t_+} and corresponding mean velocity U_{t_+} give insight on the discharge flowing beside the hull and are therefore also compared with theoretical values.

Return current U_r and waterlevel depression z_a

Kreitners schematisation (see chapter 2) gives a prediction of the return velocities as function of the hull velocities and the blockage.
The resulting equation (2.10) gives a relation between these and is used to verify the experimental results. Figure 3.18 shows the resemblance of two tests, T3.1 and T5.3 with a blockage K of respectively 17% and 4%, with Kreitners schematisation.

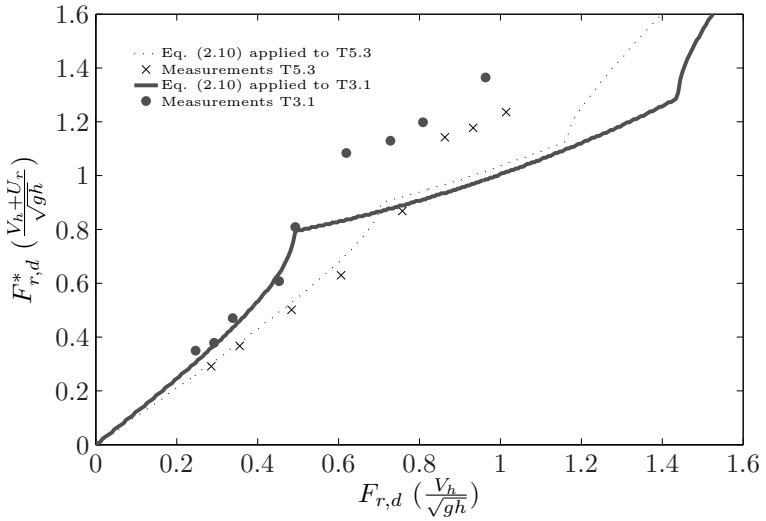

Figure 3.18: Primary wave, experimental data verified against equation (2.10).

From the figure it can be concluded that within the sub-critical domain the values correspond quite well with theory. In the trans-critical range however the return velocities as found in the experiments are much higher than theory predicts.
From momentum conservation (equation (2.2)) it can be understood that the size of the return current U_r and the water level depression z_a are interrelated. The underestimation by Kreitners schematisation of the return current therefore necessarily leads to a underestimation of the water level depression as well. This is illustrated further in figure 3.19. The measured water level depression z_a at WG 3 is considered the average water level depression in lateral direction and compared with Kreitners schematisation. The measured return current U_r is less convenient for comparison, since the EMF is located close to the wall and bottom. Measured velocities are therefore believed to be smaller than the average velocity over the cross section.

Above roughly $F_{r,d} = 0.75$ the water level depression systematically exceeds the predicted value. This is due to the difference between theoretical and the effective cross section of the canal beside the hull. Theoretically the flow is uniform in lateral direction. For large velocities however, the flow is contracted and the effective cross section decreases. The effect of this contraction is dependent on the blockage. This can be derived from the figure; the water level depression deviates more from the theoretical value for a run with high blockage (T4.1) than for a run with small blockage (T5.3). Under $F_{r,d} = 0.55$ the water level depression is overestimated by Kreitners schematisation. For such small velocities the water level depression in not constant in lateral direction, which explains the deviation. The flow pattern in both cases, a large hull moving fast and a small hull moving slowly, is sketched in figures 3.3 to 3.8 and supports this theory.
The lateral distribution of z_a confirms this pattern. Figure 3.20 shows that for high Froude depth numbers the deepest point moves toward the opposite tank wall. The non uniformity in lateral direction for small Froude depth numbers is, although present, barely visible in the figure.

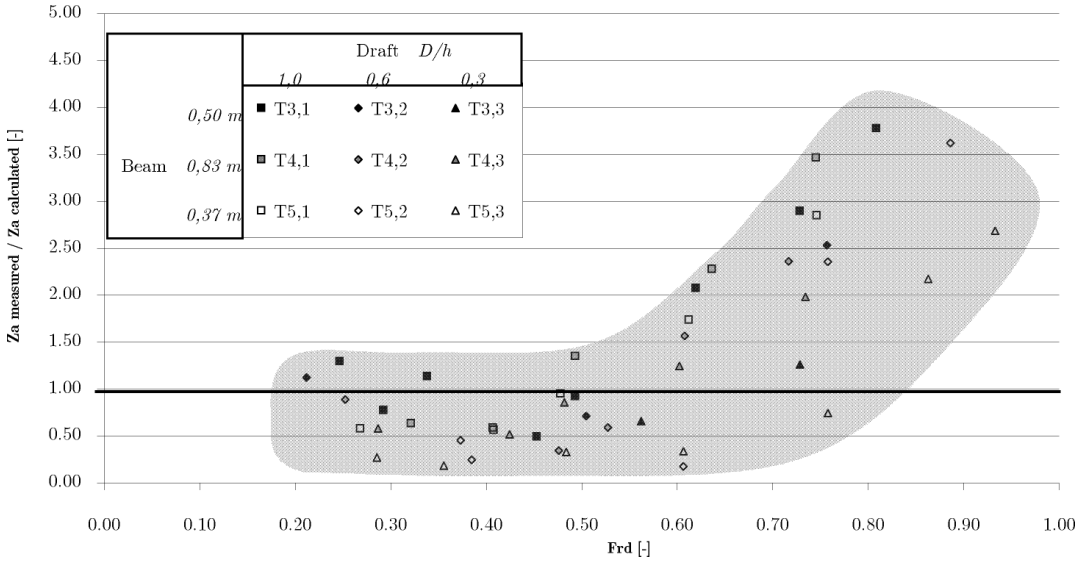

Figure 3.19: Comparison measured water level depression z_a with the theoretical water level depression according to Kreitner.

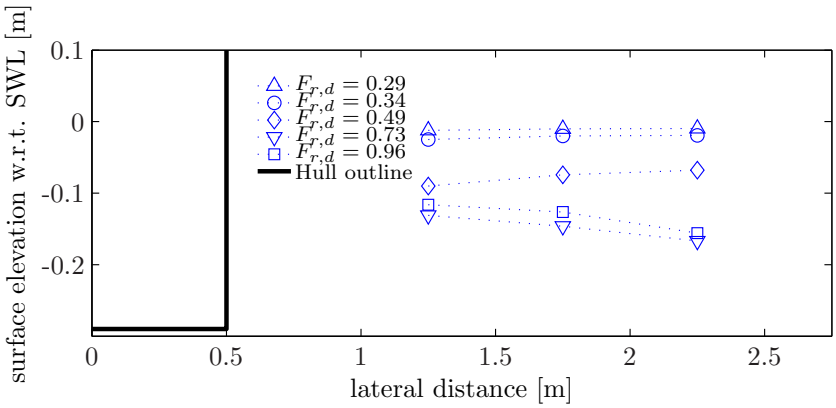

Figure 3.20: Maximum waterlevel depression z_a perpendicular to the tank axis for T3.1.

Height h_{t_+} and mean velocity U_{t_+} of the translation wave

Kreitners schematisation can also be applied to calculate the translation wave. The discharge surplus pushed in front of the hull can be calculated using equation (2.11). The corresponding height h_{t_+} follows then from (2.12). Despite the differences between return current U_r and water level depression z_a with Kreitners schematisation discussed in the last paragraph, the translation wave height h_{t_+} is a considerably well predicted (see figure 3.21). Although not shown here, mean velocity U_{t_+} has a similar resemblance with the predicted velocity.
The measured height h_{t_+} is slightly smaller than predicted, especially when the translation wave is large. When the translation wave height becomes larger than approx. 0.5 h it starts to break and the height reduces, as was observed visually and is confirmed by the figure.

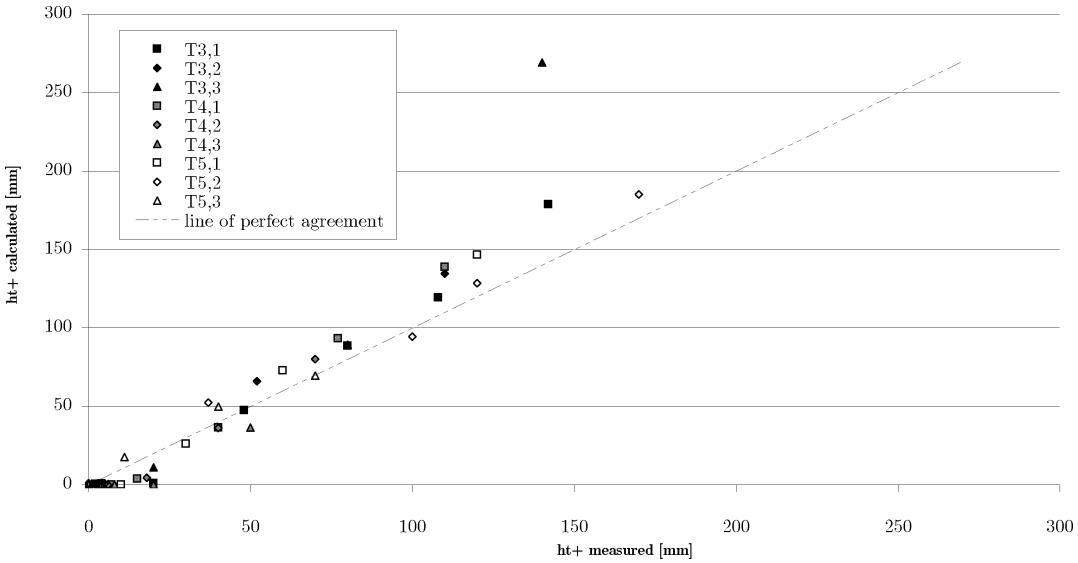

Figure 3.21: Measured and calculated translation wave height h_{t_+} compared.

The existence of a translation wave marks the trans-critical domain. The fastest sub-critical run (without translation wave) and the slowest trans-critical run (with translation wave) for each test provide an estimation of the boundary between the sub-critical ans trans-critical domain. As can be seen in figure 3.22 the test confirms the boundary as derived theoretically op page 11 (The velocity non linearity factor α_u as given by equation (2.6) is used).

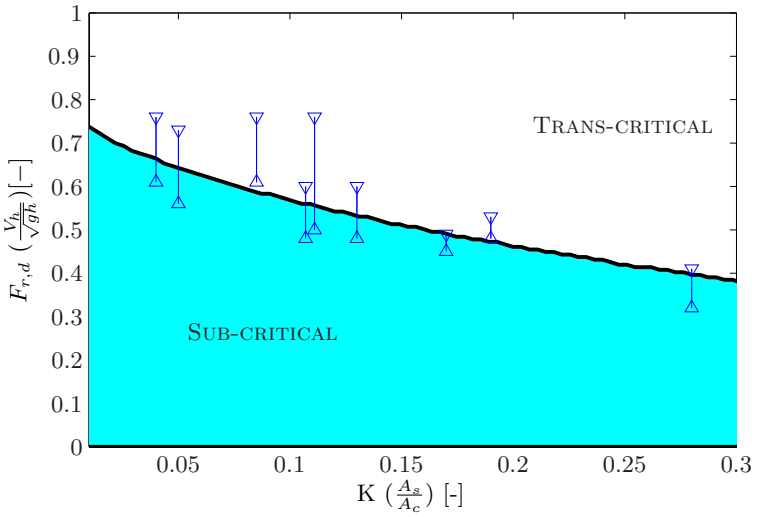

Figure 3.22: Boundary between sub-critical and trans-critical behavior. The fastest sub-critical run and the slowest trans-critical run is indicated for each test as a Δ and a ∇ respectively. Thick line represents the theoretical solution.

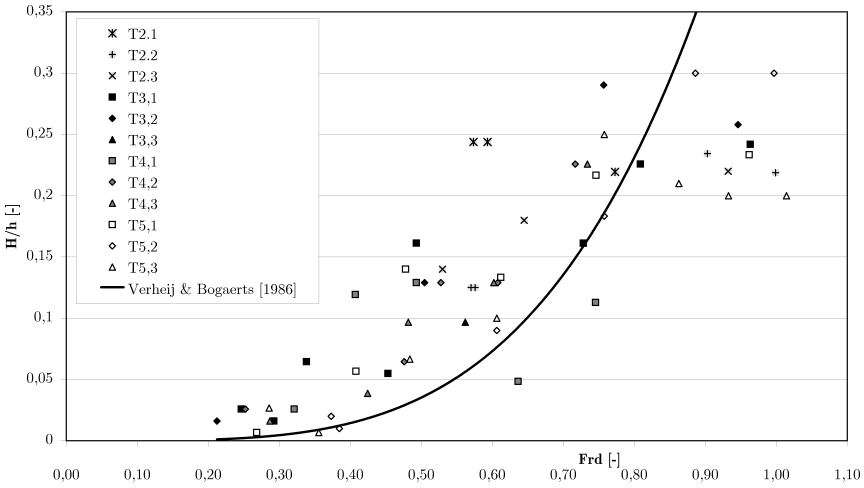

Figure 3.23: Secondary wave height, experimental data verified against (2.19).

Secondary wave pattern

Wave heights

A prediction of the height of the interference cusps is done with equation (2.19) derived in Verheij and Bogaerts (1986). Verheij and Bogaerts suggest an α_2 of 4.0 and $\alpha_1 = 1$ for a blunt object. The equation is valid for deep water conditions, generally spoken $F_{r,d} < 0.7$. The dimensionless height (H/h) of the highest interference cusp in the run is compared to equation (2.19) in figure 3.23. It can be concluded that wave heights do not exceed 0.3 times the water depth. The measured dimensionless wave height (H/h) is inadequately represented by the equation of Verheij and Bogaerts, as can be seen from the figure.
In the authors opinion this can be partly explained by the interaction between primary and secondary wave field. The secondary wave field is an interference pattern constructed beside and behind the hull. The flow condition near the hull is however to a great extent affected by the primary wave. Near the hull the velocity is increased with U_r and the water level lowered with z_a. The original formula of Verheij and Bogaerts does not take this into account.
Better results are obtained when using the local Froude depth number beside the hull ($F_{r,d} = \frac{V_h + U_r}{\sqrt{g(h - z_a)}}$) when predicting the wave height. When using this local Froude depth number the wave heights are indeed quite well predicted in the domain $F_{r,d} < 0.7$. In the trans-critical regime the secondary wave field is disturbed by large velocities beside the hull. Behind the hull a hydraulic jump disturbs the interference pattern and the measured wave heights are more scattered.
Remarkable is that the variation in the blocking has no consistent influence on the secondary wave height, and wave heights for a hull with small beam and draft (T5.3) are not smaller than for a hull with large beam and draft (T4.1).

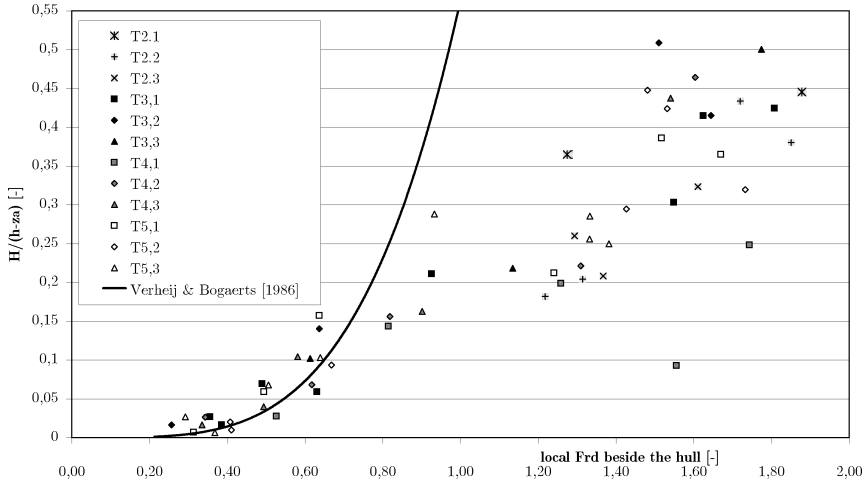

Figure 3.24: Secondary wave height, experimental data verified against (2.19), using $F_{r,d} = \frac{V_h + U_r}{\sqrt{g(h - z_a)}}$.

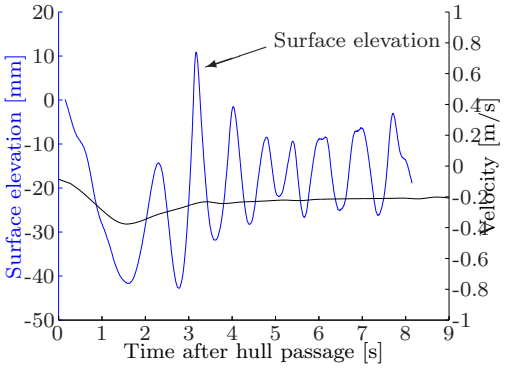

Figure 3.25: Surface elevation and longitudinal velocity after the hull passage (Run T4.2 0.92 m/s). Note: The orbital velocity is subtracted from the velocity signal with the EMD procedure used previously to separate the primary and secondary wave from the surface elevation.

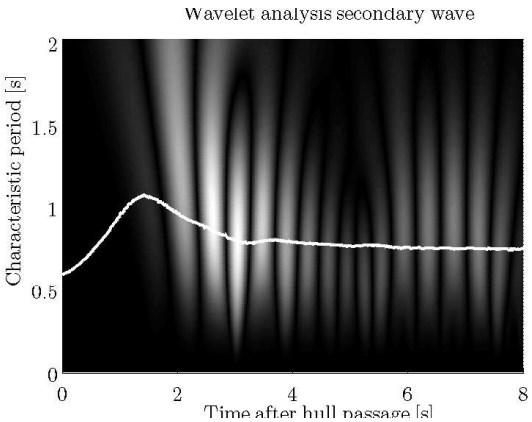

Figure 3.26: Scaleogram, lighter colors indicate high correlation, including the theoretical wave period in white (Run T4.2 0.92 m/s).

Wave periods

The measured wave periods depend beside the wave length also on the wave angle and the return velocity. The velocity underneath the secondary wave field is shown in figure 3.25. The period of the featherlet waves can be derived corresponding to the theory from appendix A and is dependent on the velocity of the vessel and the water depth. Neglecting the return current a wave period of about 0.5 s is calculated, much smaller than the observed period. In case of a return current the velocity of the hull with respect to the water increases and the wave lengths and angles increase. The run displayed in figure 3.25 has a return current velocity in the order of 0.2 m/s and the influence of the velocity on the period is made visible in figure 3.26. Figure 3.26 shows the scaleogram for the secondary wave, including the theoretical wave period calculated for a vessel moving at a speed of $V_h + U_r$. The pseudo periods vary from 1.1 to 0.8 s, matching quite well with period calculated for a vessel moving at a speed of $V_h + U_r$.

Wave angles

The measurement of the wave angles is beyond the scope of this report. According to de Vries (2007), the wave angles measured in the physical model are around 55 ° in the sub-critical domain. This corresponds with the theoretical derived wave angle.

3.5 Conclusions

The basic phenomena described in chapter 2 are confirmed by the physical modeling, especially in the deep water domain ($F_{r,d} < 0.7$).
Within the deep water regime the primary wave and secondary wave are can quite well be predicted separately using existing theories (Kelvin, Kreitner, Verheij and Bogaerts). The primary wave is relatively small, the return current is negligible and the secondary wave pattern is created in nearly still water.
The maximum wave height is found to be around 0.3 times the water depth at $F_{r,d} = 0.7$. No direct relation between the blockage and the secondary wave height is revealed. When hulls with a blockage of 4% and 26% are towed with the same velocity the wave heights are of the same order. In case of a large blocking of the cross section it is recommended to include the influence of the small return current and water level depression and taking the local Froude depth number when calculating the wave height.
In the trans-critical range conservation laws are less applicable. The flow contracts beside the hull, leaving a small gap for the flow. This leads locally to high velocities especially when the blockage is high. Kreitners assumption of energy head conservation and uniform velocities and water levels are less valid once the speed increases into the trans-critical range.
The velocity beside the hull eventually becomes super-critical and a hydraulic jump is formed after the hull once the flow diverges and decelerates. In case of large blocking and velocity a classical hydraulic jump (also called a bore) is generated. If the velocity is however only slightly super-critical beside the hull, a undular jump is formed. In this regime it is unclear whether the waves seen behind the vessel are a part of this undular hydraulic jump or the secondary wave field.
The trans-critical domain should be avoided in a wave pool design since the high velocities are considered to hinder the surfer as well as the construction of

a clean secondary wave pattern. The boundary between sub-critical and trans-critical domain can be well predicted.

4

Numerical model study

Testing in a physical model is quite costly, especially regarding such a complex design. Numerical modeling can often be an asset, since changes in the design can be implemented relatively easy once the model is finished.
In the following chapter the possibilities of modeling the problem numerically are discussed and different types of modeling are compared to the experiment and theory of the previous chapters.

4.1 Introduction

Computational modeling of flow is solving its basic conservation laws. The behavior of the flow can be described by conservation of mass and the conservation of motion in all directions. The equations of motion (Newton's second law) are derived and elaborated upon in numerous publications. A good description can be found in Lamb (1932) and Stoker (1957). The equation of motion in one of the most general form (Navier Stokes equation) for a fluid is given by:

$$\rho \frac{D\vec{u}}{Dt} = -\nabla p + \nabla T + F. \tag{4.1}$$

With ρ, the density of water [kg/m^3],
$\vec{u}$, the velocity vector $(u, v, w)^T$) [m/s],
∇, the vector divergence operator ($\nabla = \frac{\partial}{\partial x} + \frac{\partial}{\partial y} + \frac{\partial}{\partial z}$),
∇p, the pressure gradient [N/m^3],
∇T, the viscous shear forces [N/m^3] and
F, the external forces [-].

This can be solved once combined with the equation of mass conservation. Mass conservation is given by:

$$\frac{\partial \rho}{\partial t} + \nabla \cdot (\rho \vec{u}) = 0. \tag{4.2}$$

The difficulties in solving these equations lie in the broad range of scales that have to be solved non linearly. The small scale structures such as turbulence influence the larger scale motion, and for a good representation their influence should be included. Solving however the full non linear set of equations from the smallest scales up to the wave pool scale remains impossible with the current computer power. Therefore computational fluid mechanic packages simplify parts of the equations to model flow, neglecting or simplifying terms in equations (4.1) and (4.2).
The applicability of a model lies within the simplifications it is based on, as will made clear in the upcoming sections.

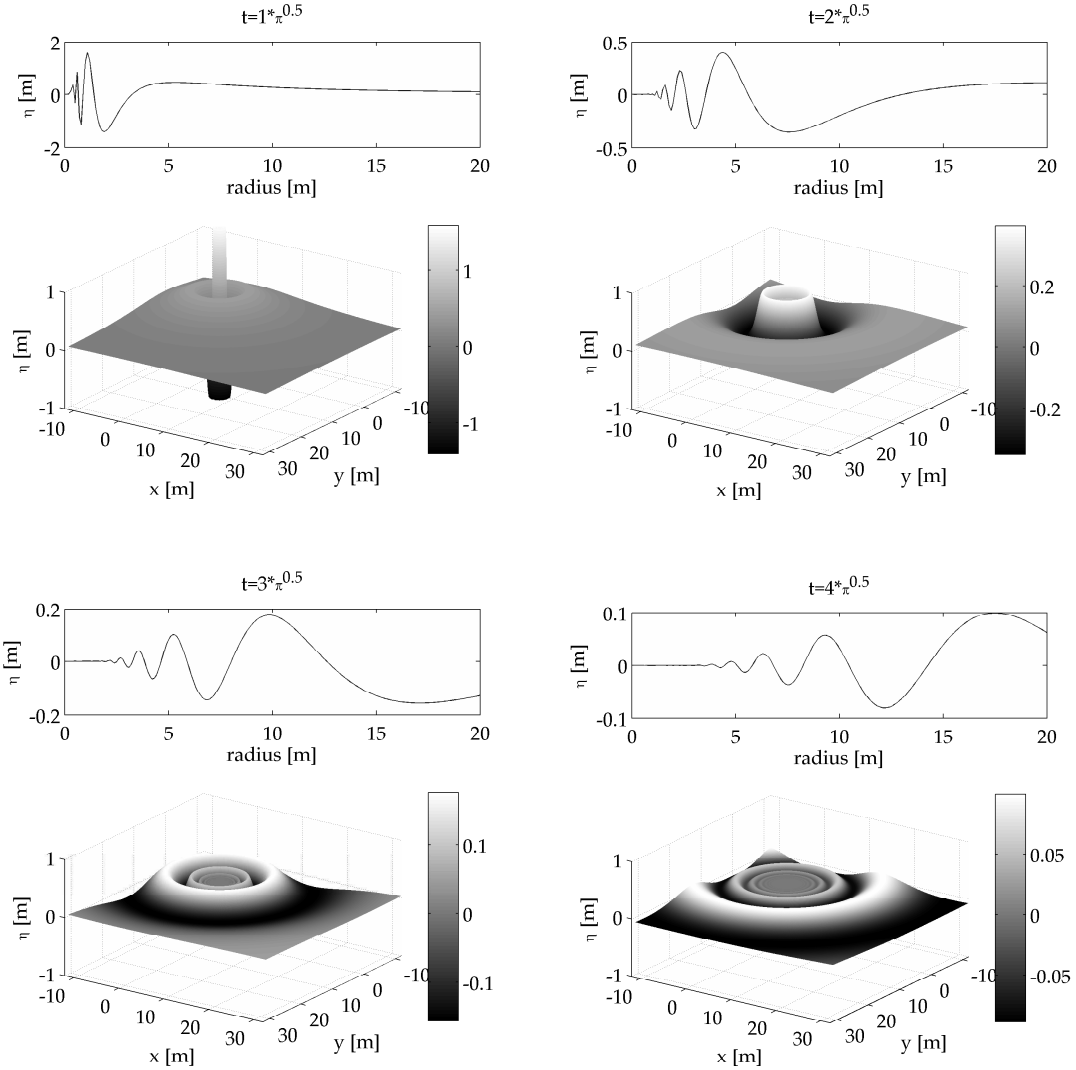

Figure 4.1: Waves radiating out of the origin after a initial disturbance.

4.2 Pressure point modeling

Method

The secondary wave field is commonly referred to as the result of a moving pressure point. Pressure point modeling is based on that assumption. The ship is modeled as an infinitely small pressure point moving in a infinitely large domain. In the following section the validity of this method is examined.

The radial wave pattern from a pressure point is well known and mathematically defined. It concerns waves radiating out into a medium after a short impulse on $t = 0$, comparable to waves after a stone is thrown into water (figure 4.1). The changing cross section of a ship causes gradients in the flow, which generates waves, as mentioned in the previous chapters. It is this excitation of the flow when accelerating past the hull that is comparable with the short impulse of a pressure point.

The pressure point model is based on so called potential flow. When assuming potential flow equation (4.1) is highly simplified. The basic assumptions will be mentioned hereunder, without going into all the mathematical details.
First of all potential flow is based on the assumption that water is **incompressible**, valid for most free surface problems since the bulk modulus of water is 2.2 $.10^9$ Pa. In case of an incompressible and Newtonian fluid the viscosity ∇T is then proportional to $\nabla^2\vec{u}$. For flow with small gradients, the term $\nabla^2\vec{u}$ is at least an order smaller than the other terms, and this second order term can be removed, assuming the fluid **inviscid**. It is further assumed that the flow is **irrotational**, no vortices are formed in the flow, and **divergence-free**, no mass is generated or dissipated in the volume. Then and only then, the flow can be described as potential flow. And since the flow is assumed to be inviscid and irrotational, potential flow cannot be applied for locations with large spacial variations in the velocity, such as a boundary layer.
With potential flow it is possible to derive a mathematical description of the surface elevation after a short impulse in the origin. According to Lighthill (1978) the surface elevation η_p in time and space is given by:

$$\eta_p(r,t) = c\frac{\sqrt{\pi}}{r}\sqrt{\frac{gt^2}{4r}}\exp\left\{-a\frac{gt^2}{4r}\right\}\sin(\frac{gt^2}{4r}+\frac{\pi}{4}). \tag{4.3}$$

With r, the radial distance to the origin [m],
t, time after the initial disturbance [s],
c, the strength of the impulse [m^2] and
a, the decay rate [-].

The behavior of this function is illustrated in figure 4.1.
Equation (4.3) consists of sinusoidal part ($\sin(\frac{gt^2}{4r}+\frac{\pi}{4})$), which is oscillating with increasing frequency. A point with arbitrary r will therefore encounter first the longer waves followed by the shorter ones.
Moreover, the equation contains a linear increasing part ($\sqrt{\frac{gt^2}{4r}}$) as well as an exponential decreasing part ($\exp\left\{-a\frac{gt^2}{4r}\right\}$). Close to $t = 0$ the exponential part is of minor importance and the wave heights increase in height. The increase in wave heights is followed by a rapid decrease when the exponential function approaches zero for $t \to \infty$.

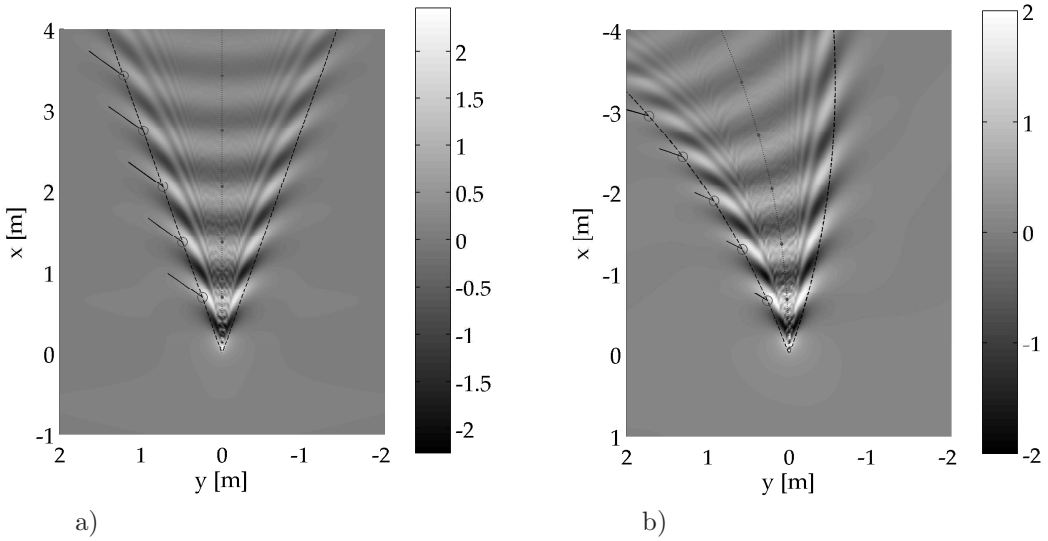

Figure 4.2: Interference pattern for a ship traveling with $1m/s$ in a straight course (a) and an arc with $R = 10m$ (b). Dashed lines represent the interference pattern as derived by Kelvin.

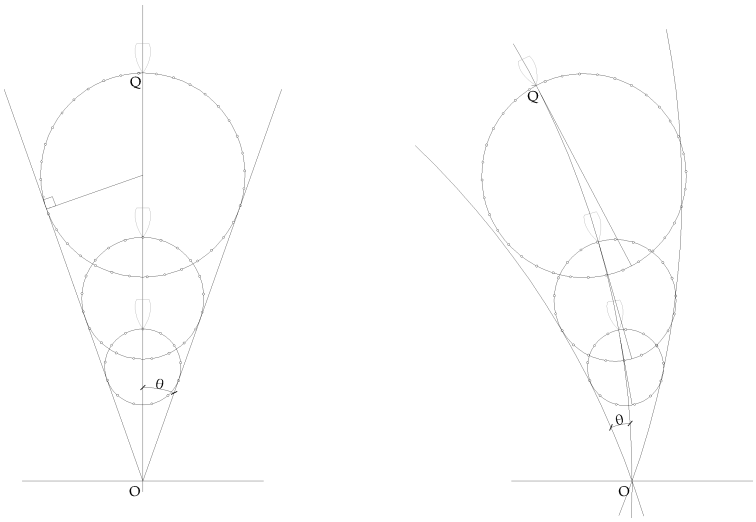

Figure 4.3: Reconstruction of the secondary wave pattern, interference circles and lines of $\theta = 19.5°$ w.r.t. the (local) sailing line angle. Note that for a straight course the circles are confined by the $\theta = 19.5°$ lines (*left*). For a circular course the $\theta = 19.5°$ lines are only tangent to the circles in the vicinity of the origin.

Hence at a fixed location one first observes long small waves followed by higher waves with a shorter wavelength and finally small ripples with even shorter wavelength .
Note that for the derivation of equation (4.3) the domain in taken infinitely large. In shallow waters the wave speed is dependent on both wavelength and waterdepth, and surface elevation cannot be described by this single equation.

Results

Theoretically the secondary wave field on deep water can be constructed by projecting and summing the point sources all along the trajectory of the vessel. Since the strength of the point source c is is a user picked value, the absolute wave heights cannot be determined. Relative wave height distribution however show the locations of positive interference (featherlet waves).

For a vessel moving in a straight line from Q $(x = -vt, y = 0)$ to the origin this can be denoted as:

$$\eta(x,y) = \int_{t=-\infty}^{t=0} \eta_p(\sqrt{(x-vt)^2+y^2}, t)dt. \tag{4.4}$$

When equation (4.4) is discretized and integrated indeed a secondary wave V-pattern emerges. Interference angle $\theta = 19.5°$, wave angle $\phi = 55°$ and wavelength as derived in appendix A are modeled accurately. For vessel speed $v = 1m/s$ the pattern as well as this theoretical solution are depicted in figure 4.2.a.

A ship following a circular course is modeled similar. The point sources are projected on a curved sailing line. In the region close to the origin the wave and interference angles are presumed to be the traditional $\phi = 55°$ and $\theta = 19.5°$ with respect to the local sailing line angle. For waves close to the origin the path is relatively straight and the interference is identical to a straight sailing vessel. Further away from the origin the pattern must deviate slightly since the interference angle is the tangent along all interference circles (appendix A). A reconstruction of the pattern (figure 4.3) illustrates that the only in the vicinity of the origin the interference line be predicted by $\theta = 19.5°$. For wide curves the first interference cusps (featherlet waves) lie within this region.
The outcomes of a computation of a pressure point moving on a circular path is depicted together with theoretical solution in figure 4.2.b.

In summary, the secondary wave field can quite well be predicted using a summation of pressure points. The interference angle $\theta = 19.5°$, wave angle $\phi = 55°$ and wavelength are represented correctly. Moreover these values appear to be valid for ships moving in a circular course with relatively a large radius. Close to the vessel the pattern then corresponds to the traditional wave pattern bended along the sailing line.

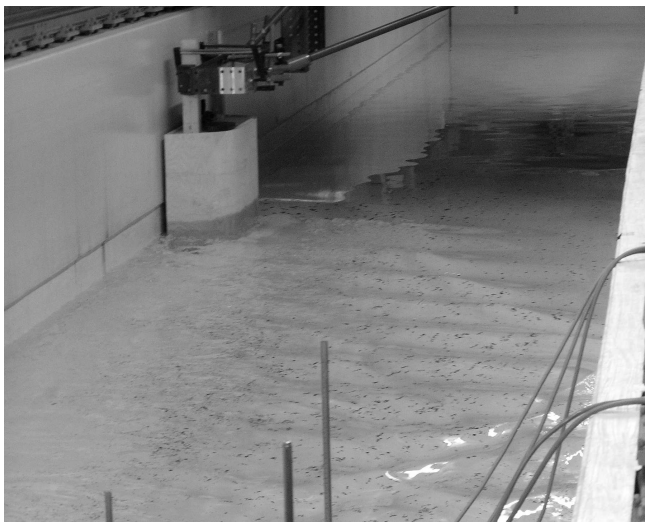

Figure 4.4: Wave field behind the hull (Run 5.1 0.82 m/s). The waves are reflected in the lower right corner of the image.

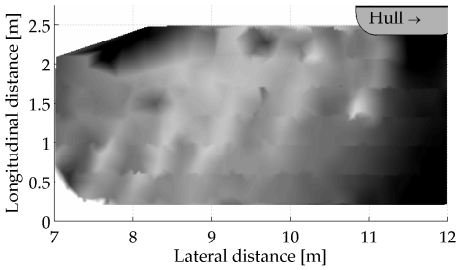

Figure 4.5: Surface elevation as derived from stereo photogrammetry (Run 5.1 0.82 m/s). Lighter colors indicate higher surface elevations. Absolute surface elevations are not derived for this run, the relative elevation however indicates the wave angle. Data courtesy of de Vries.

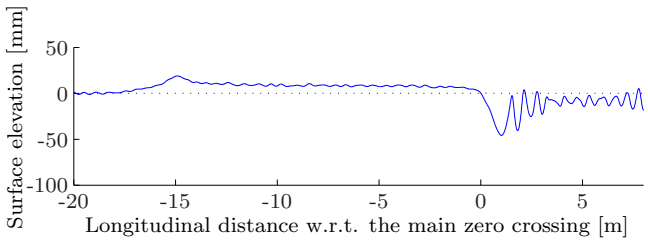

Figure 4.6: Measured surface elevation WG2 at 0.88 m from the hull (hull moving from right to left)(Run 5.1 0.82 m/s).

4.3 Panel method modeling

Method

The pressure point modeling prescribes the secondary wave pattern in a qualitative way. To observe the flow closer to the hull a panel method is used.
A panel method computes the fluid motion at its boundaries by dividing these surfaces into panels. Here the *DELKELV* panel model developed by de Koning Gans at the faculty of Mechanical Engineering and Maritime Technology (Delft University of Technology) is used and its basic assumptions will be discussed hereunder. The mathematical background of the model is described in de Koning Gans (1992).

The basis of panel methods is Green's identity. It states that the volumetric differential describing the potential flow can be transformed in a two dimensional integral. In simple terms, the three dimensional fluid behavior can be computed by modeling it's boundary surfaces.
The *DELKELV* model computes a stationary potential flow field by discretizing these surfaces into panels. Panels radiate disturbances with unknown strength into the medium and the model computes all panel strengths while complying with potential flow equation and its boundary conditions. These boundary conditions restrict the flow, for instance to be tangential to the hull or free surface.

Further the coordinate system is transformed, such that water flows with a velocity V_h towards a fixed vessel. The flow around the object is then decomposed by means of $u = \bar{u} + u'$ into a known base flow $\bar{u} = V_h$ and small perturbations u'. These small perturbations are linearized assuming both $u' << \bar{u}$ and $u'^2 << \bar{u}u'$.
This linearisation of the velocity perturbations makes the ship building panel method unsuitable to design a hull with maximum wave generation. This can be made clear by examining how the kinematic boundary condition at the free surface is determined:

$$\frac{\partial \zeta}{\partial x} = \frac{w}{\bar{u} + u'} \; linearized\, to \; \frac{\partial \zeta}{\partial x} = \frac{w}{\bar{u}}. \tag{4.5}$$

For slender ships this assumption holds, however the wave pool hulls are to be rather blunt to maximize the waves and u' cannot be neglected. The *DELKELV* model thus cannot be used to optimize a hull shape due to the assumptions it is based on. Within the sub-critical region (with a stationary solution) however the model can be compared to the experiments.

Results

As discussed in the previous chapter, most runs during the experiment were in the trans-critical region and had a translation wave preceding the hull. A run with a minimal translation wave is selected since the model cannot reproduce the translation wave.
The smallest hull with a beam of 0.38 cm (test T 5.1) is modeled with water flowing at $F_{r,d} = 0.48$ past by. Although theoretically in the sub-critical domain, a small translation wave of about 10 mm is measured before the hull. An overview of the wave field and the wave angles is depicted in figures 4.4 and 4.5. Waves have an angle of about 60 ° with the sailing line and are reflected by the tank wall. The wave gauge signal 0.88 m from the hull is depicted in figure 4.6.

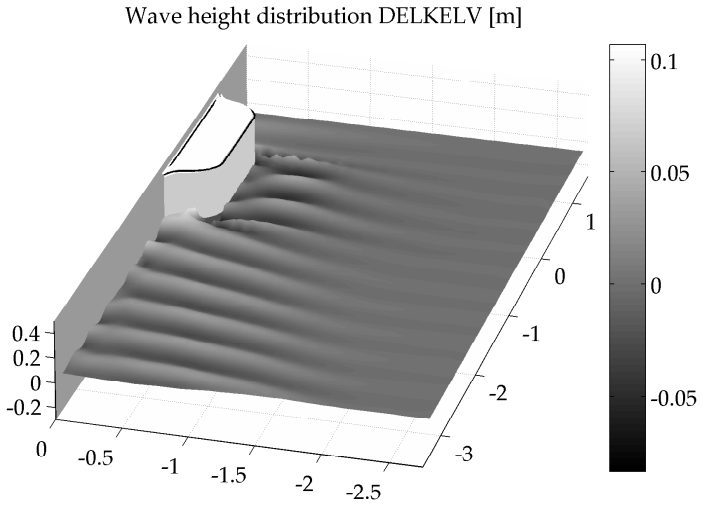

Figure 4.7: Wave field behind the hull *DELKELV* computation (Run 5.1 0.82 m/s).

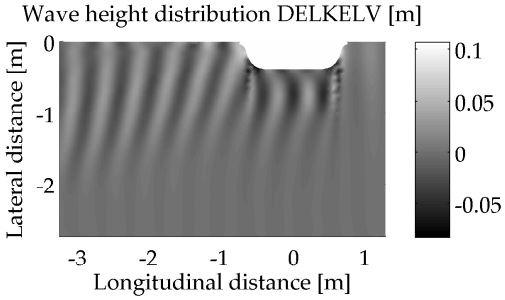

Figure 4.8: Top view wave field behind the hull (hull moving from left to right).

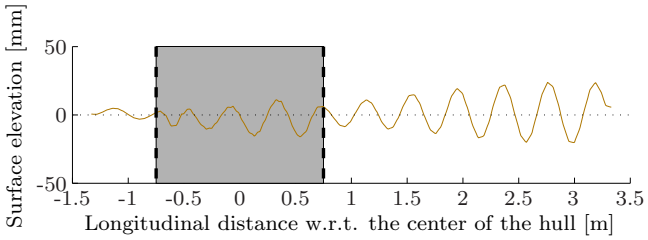

Figure 4.9: Calculated surface elevation at 0.88 m from the hull (*DELKELV*) (hull moving from right to left).

The experiment is reconstructed including the tank wall and bottom in the panel model. The hull is rounded off slightly, to prevent instability, and the problem is modeled with the maximum amount of panels possible. An overview of the wave field behind the hull is given in figure 4.7. Some differences are visible from the figure. Directly behind the hull the flow detaches and forms a highly turbulent region with hardly any waves as can be seen from the photograph. Since the model is based on potential (inviscid and irrotational) flow, this region cannot be represented right, and indeed the model predicts high waves behind the hull. Furthermore figure 4.4 shows reflected waves from the tank wall which cannot be seen in the model.
This can be further illustrated in a top view (figure 4.8). In the model the wave angle is about 75 ° and the wave angle increases to 90 ° near the wall, and since these wave propagate parallel to the wall no reflection is modeled. A wave angle of 60 ° was measured in the experiment, and since waves approach the wall oblique, a reflected wave field as well.

The surface elevation as measured during the experiment is depicted in figure 4.6. The small translation wave of 10 mm is visible and a local water level depression z_a beside the hull of 42 mm. Next, 3 clean waves of about 40 mm followed by a the turbulent region with irregular ripples. In a cross section of the model outcomes at the location of the wave gauge (figure) the local water level depression is hardly visible and wave heights are about 40 mm. When investigating the model results further, the return currents are found to be negligible. The wavelengths in the model are 0.45 m, indeed perfectly matching the theoretical wavelength for a domain without return current. But since in the experiment the waves are generated in field with a small return current, the waves elongate slightly, and the measured wavelengths are 0.60 m.
When reflecting on the assumptions, it can be stated that the basis of the linearisation of the velocities, $u' << \bar{u}$, is not valid in case of the wave pool. Close to the hull u' and v' are only three times smaller than the base flow velocity $\bar{u}$ and hence their influence cannot be neglected.

So in summary, a panel method as *DELKELV* cannot be used to optimise the hull for the Liquid Time Wave Pool. The influence of the restricted domain, the walls and bottom, is not represented accurately. Because the water level setdown z_a and return current U_r are not accurate, the secondary wave field deviates as well. Nevertheless *DELKELV*, being accurate for slender bodies in unrestrained waters, is a excellent tool to generate a validation dataset for more complex models.

4.4 3D modeling

The most advanced models solve the full Navier Stokes equations (with a simplified turbulence term) in all directions. Non hydrostatic flows are possible since the equation of motion is computed in the vertical direction. The same run as the used in the previous section, run T 5.1 0.82 m/s, is modeled with a Navier Stokes solver *FINLAB* of R.J. Labeur, partly developed at the University of Technology Delft. Modeling the flow beside the hull has appeared to be quite difficult.
Some of these difficulties are:
It is common practice to transform the coordinate system, setting the hull fixed in the domain and having only water moving with in the domain. The inflow is then set at $\bar{u} = V_h$. However, when a translation wave is generated it will propagate across the boundaries, which then becomes poorly defined. Consequently, it is required to have the hull moving,

with all the difficulties of changing the computational grid each time step. Like with the panel method modeling, it is necessary to smoothen the sharp edges of the hull for stability. The secondary wave field is the result of numerous point sources, and the interference pattern emerges when the contributions of all these are computed. In both pressure point model and panel method radiating sources are basis of the solution by definition. For a Navier Stokes solver however to represent the (changing) wavelengths of a point source, a very small grid size and time step is necessary because the interference pattern can only be calculated correctly when the dispersion relation for each component is computed accurately.
Despite the effort it has until now not been possible to reproduce the experiments correctly (figures 4.10 and 4.11). A prominent difference with the physical experiment is seen when comparing the cross sections in figure 4.6 and 4.11. The water level depression is overestimated with a factor 2 by the model. Furthermore the wave crest turn perpendicular to the tank wall, where in reality the waves approach the wall oblique and are reflected (the *DELKELV* model showed a similar imperfection).

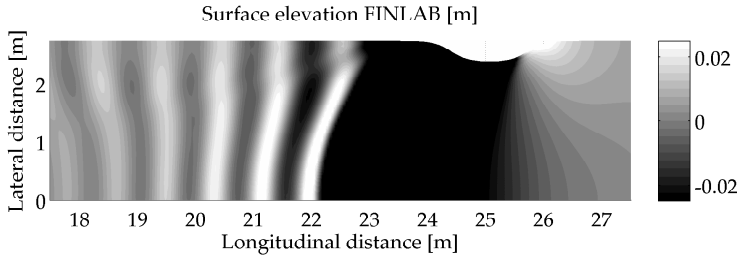

Figure 4.10: Calculated surface elevation (*FINLAB*) (T5.1 0.82 m/s).

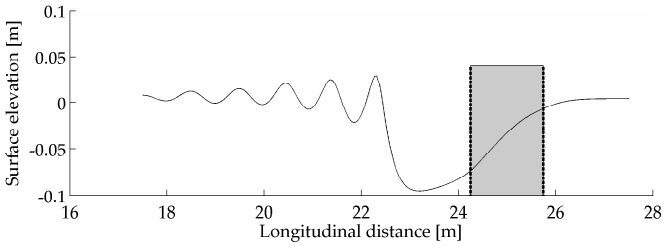

Figure 4.11: Calculated surface elevation at 0.88 m from the hull (*FINLAB*) (T5.1 0.82 m/s).

4.5 Conclusions numerical modeling

Numerically modeling the wave pool as a whole in all its interesting aspects would be ideal. With the current state-of-the-art models that is not possible yet. The complexity of the problem lies in the combination of moving objects, both sub-critical and super-critical flow, breaking waves and the accompanying currents. Even if current models would be able to compute the flow of such a complex nature, the validity of the outcomes would remain unknown.

With a Navier Stokes solver *FINLAB*, it has not been possible to reproduce the towing tank outcomes.
A panel method such as *DELKELV*, although very useful in maritime engineering, is not the appropriate model for a hull maximizing the wave height. Nevertheless, for the further development of *FINLAB*, it can generate validation data for slender ships on deep water.
The pressure point model has proven that the wave angles with respect to the sailing line are identical in case of a ship moving in a wide circular path and a straight sailing line. This is used in the further design of the wave pool and the computation of the wave crest in the following chapter.

5
Wave pool design

The conclusions of the previous chapters are applied in the evaluation of the Liquid Time Wave Pool concept.

5.1 Design evaluation method

The Liquid Time concept is based on 2 m waves for intermediate to expert surfers. This wave height is the basis for the design. A peel angle of about 40 degrees is then required as can be deducted from Hutt's classification (Chapter 1).
The surfable wave is the part of the secondary wave. Wave heights increase with increasing hull velocity (or $F_{r,d}$) until the hull enters the trans-critical range and the secondary wave field becomes disturbed by the high velocities beside the hull. From the physical modeling it was concluded that the maximum wave height over water depth ratio H/h is between 0.25 and 0.3. The wave angle with respect to the sailing line is 55 ° for Froude depth numbers $F_{r,d} < 0.6$ and increasing towards 90 ° if Froude depth numbers approach one. Close to $F_{r,d} = 1$ the secondary wave field is however hardly visible, because the strong return current forms a hydraulic jump behind the hull. The boundary of the trans-critical domain is determined by the blockage, the ratio between the cross section of the ship and the canal (see figure 3.22). The wave angles with respect to the sailing line are close to the origin identical for a vessel moving in curved course with a large radius as for a vessel moving in a straight line. Based on this assumption a refraction model of the wave pool is setup to predict the location of the wave crests. Refraction, shoaling and wave breaking are computed as elaborated on in page 17 to 21.

Table 5.1: Liquid Time initial wave pool design

Radius outer wall pool	100	m
Water depth generation area	3	m
Width generation area	13	m
Length slope	18	m
Bottom slope	1:6	
Cross section canal	68	m^2
Cross section hull	≈10	m^2
Blockage K	0.147	
Hull speed in $F_{r,d}$	1.0	
Hull speed	5.42	m/s
Wave height generation area $H/h = 0.3$	≈ 0.9	m
Wave angle featherlet waves ϕ	90	°
Wave length featherlet waves	65	m
Wave period featherlet waves	12	s
Predicted peel angle	34	°
Refraction factor K_r	1	
Shoaling factor K_s eq. (2.28) very shallow water	1.3	
Predicted wave height at breakpoint H_b	1.17	m

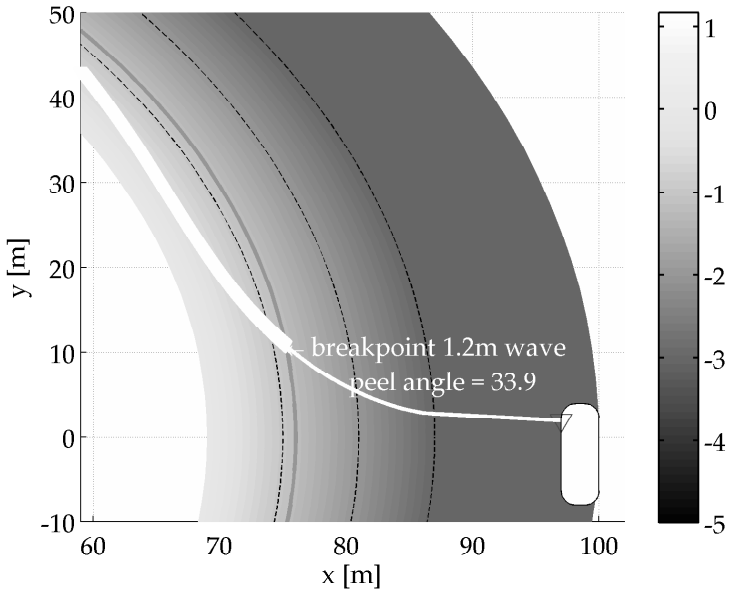

Figure 5.1: Wave crest refracting in the initial design. Colors indicate water depth in m, dashed lines are the 1, 2 and 3 m depth contours and the white rectangle in the lower right corner represents the hull.

5.2 The Liquid Time initial design

The initial wave pool design described in chapter 1 is evaluated with the design criteria mentioned in section 5.1. The cross section of the wave pool is described in table 5.1.
In the initial design with a cross section of about 10 m^2 is placed in a pool relatively small cross section and towed at $F_{r,d} = 1.0$. The combination of the large blockage and towing the hull at $F_{r,d} = 1.0$, will lead to a large translation wave in front and a hydraulic jump after the hull. Furthermore high velocities in the order of 3 to 4 m/s are expected, making it difficult for the surfer to stand up (since the water moves 8 m/s (30 km/h) with respect to the hull and its wave field).

Wave height is estimated to be in the order of a meter, because the water is too shallow for the required 2 m waves. The refracted secondary wave crest is illustrated in figure 5.1. The wave has an angle of almost 90 ° with the sailing line and therefore the refraction factor K_r is undefined. A $K_r = 1$ is chosen, suggesting no decrease in wave height due to refraction. Noted that is is unlikely that the wave crest will fully refract on such a short slope. The wave angle at breakpoint is underestimated by the refraction model.

The generation of secondary waves is nevertheless suppressed by a hydraulic jump behind the hull and only a hydraulic jump will be visible.

So, in summary, the initial design is not satisfactory since it induces a large translation wave, fierce return currents and a wave height smaller then sought after.

Table 5.2: Liquid Time amended wave pool design

Radius outer wall pool	100	m
Water depth generation area	7	m
Width generation area	20	m
Length slope	20	m
Bottom slope	1:4	
Water depth at end of the slope	5	m
Cross section canal	190	m^2
Cross section hull	≈10	m^2
Draft hull	3.5	m
Beam hull	3	m
Blockage K	0.052	
Hull speed in $F_{r,d}$	0.7	
Hull speed	5.8	m/s
Wave height generation area $H/h = 0.3$	$\approx$ 2.1	m
Wave angle featherlet waves ϕ	60	°
Wave length featherlet waves	16.3	m
Wave period featherlet waves	3.5	s
Predicted peel angle	42	°
Refraction factor K_r	0.87	
Shoaling factor K_s eq. (2.26) shallow water	0.93	
Shoaling factor K_s eq. (2.28) very shallow water	1.09	
Predicted wave height at breakpoint H_b	1.9	m
Predicted breaker type ξ	0.6	(plunging)

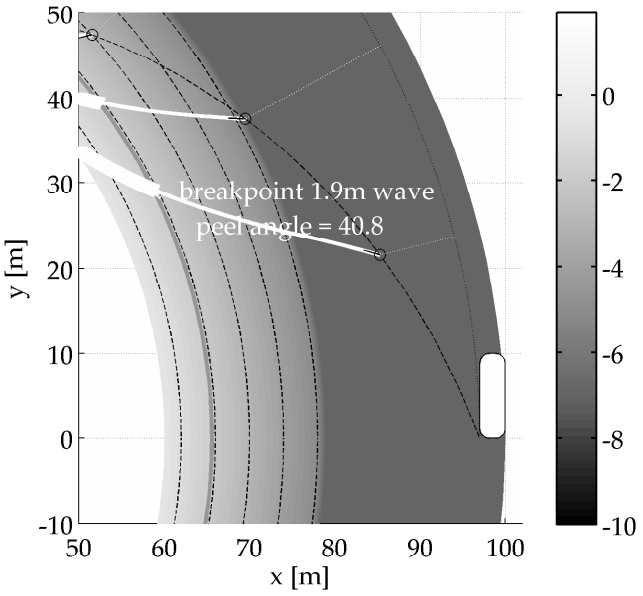

Figure 5.2: Wave crest refracting in the amended design. Colors indicate waterdepth in m, dashed lines are the 1, 2, 3, 4 and 5 m depth contours on the slope and the white rectangle in the lower right corner represents the hull.

5.3 Amended design

To prevent the difficulties in the trans-critical domain it is suggested to reduce the blocking and the speed. Furthermore the water depth is increased to 7 m in the generation area. Beside that a large water depth is required for the 2 m wave, it is also necessary to reduce the blocking.
The hull size remains about 3 by 3 m which, if compared to inland waterways vessels, must be able to generate the 2 m waves.

The inner slope of the pool has a slope of 1:4, to generate plunging waves. When a depth of 5 m is reached the slope drops to 7 m. The wave generation area is hence large and deep, minimising the strength of the return flow.

A prediction of the wave crest location is computed and depicted in figure 5.2. As shown in the numerical modeling is it legitimate to calculate the wave angles with respect to the local sailing line the ship moves in a wide arc.
First the full wave pattern is calculated for a ship moving at 5.8 m/s in a water depth of 7 m on a circular path with radius of 97 m. Next, the featherlet waves are refracted with linear refraction theory (equation (2.22)). The shoaling is calculated with linear theory (equation (2.26)) followed by non linear theory (equation (2.28) in very shallow water ($h < 2.7\ m$). The computation does not account for the length of the crests nor the amount of waves. The purpose of the computation is to estimate the peel angle. A peel angle of about 40° is found, providing an exciting ride for a surfer.

The reduction of the blockage reduces the velocities around the hull and an undisturbed secondary wave pattern is expected. This confirmed by the physical model study in chapter 3. A run with similar blocking and velocity (Run T5.3 1,4 m/s. see table 3.1) is investigated. A hull with a blocking of 0.04 is towed with a measured Froude depth number of $F_{r,d} = 0.76$. The secondary waves are about 75 mm high and the wave angle is 61 °. The waveguage signal of WG4 (for the wavegauge position see figure 3.2) is depicted in figure 5.3.
The primary wave is small in size since the blocking is relatively small, and a waveheight over waterdepth ratio H/h of 0.25 is measured. A small translation wave with an average height of 10 mm is visible, only a fraction of the secondary wave height.
If scaled by a length scale of 1:23 this would imply at full scale in 7 m water depth a measured wave height of 1.75 m at about 50 m from the hull.

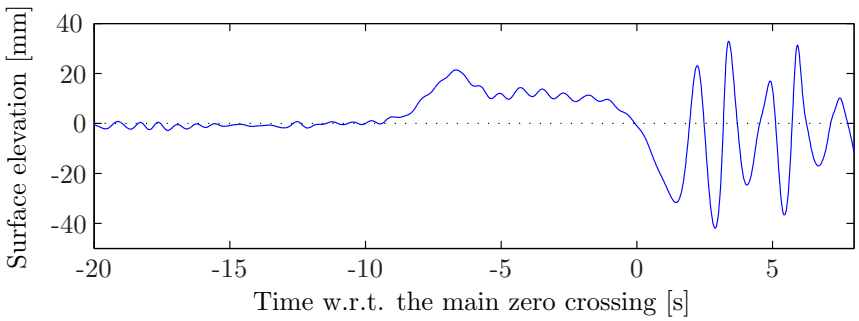

Figure 5.3: Surface elevation 1.88 m from the hull(WG4)

6 Conclusions

The objective of this study was to comprehend the physical phenomena of waves in a circular pool with hulls as wave makers, and evaluate the Liquid Time project. Both objectives are evaluate in the upcoming sections. The conclusions and recommendations are interrelated, since both objectives originate from the same wave pool concept.

6.1 General conclusions and recommendations

During this study a physical experiment is executed and compared to the existing theory. Within the sub-critical domain the existing theories about water level depression, wave length and wave angle have proven to be accurate. Exact formulas predicting the height of the waves are not available. Wave heights can be estimated using the formula of Verheij and Bogaerts, in which the exact shape of the vessel is of minor importance.
The maximum wave height H is limited by the water depth h. A maximum wave height of 0.3 times the water depth ($H = 0.3\,h$) is found in the physical model. In the sub-critical domain no significant difference in wave height is found between hulls of different blockages.

In the trans-critical domain the surface elevation is less predictable, since the flow is non uniform. The surface elevation in this domain is dominated by the primary wave and an undular or classical jump is formed behind the hull. The lack of knowledge of the trans-critical flow can be explained, since ordinary self propelled vessels avoid this region. In future research it is therefore interesting to investigate the dis(similarities) between the undular jumps in trans-critical flow and the secondary wave field in sub-critical flow, since both originate from gradients in the flow.

The influence of the curved outer wall still has an unknown effect. The interference causing the featherlet waves is altered since the curved wall focuses the waves slightly. To what extent the wave height and angle are changed is subject for future research.

This study is restricted to a fairly simple hull shape. It is suggested to investigate different positions of the blocking object. Can for instance, a similar wave field be generated by an object towed over the pool floor?

Furthermore the possibilities of modeling the phenomena numerically was investigated. It is concluded that a numerical model which includes wave generation by a hull in shallow water, the wave breaking on the slope and the generated currents is not available yet. It is recommended to validate first a existing numerical model, such as *FINLAB* (page 53), on a more straightforward case, and develop the capabilities from there.

6.2 Conclusions and recommendations with respect to the project

The initial design as discussed in 1.2 is evaluated with the knowledge of theory, physical and numerical model study. It was concluded (see section 5.2) that the large velocity ($F_{r,d} = 1$) will cause a translation wave and large return currents, since it is within the trans-critical domain. Furthermore the 3 m water depth in the generation is insufficient to generate the desired 2 m waves, since a maximum wave height over water depth ratio is 0.3.

An amended design is presented in chapter 5. Water depth is increased to 7 m and the generation area is enlarged to reduce the blocking to 5%. The large generation area causes a weak return current and as less turbulence in the pool as possible. In such a cross section it is technically possible to generate 2 m surfable waves by towing a hull in the sub-critical range ($F_{r,d} = 0.7$).

Within the timespan of this project it is more reasonable to make use of physical models, since numerical models are not capable to compute all aspects of the wave pool yet. It is therefore recommended to make a scale model of the wave pool. The scale is suggested to be at least 1 : 20, preferably 1 : 10, to reduce the influence of scale effects, as elaborated on in 3.1.

Within a scale model it suggested to study the following design elements:

- **Hull Shape**. Within the scope of this master thesis, it wasn't possible to investigate different hull shapes. Hull shapes can have a large influence. However a 3 m wide hull with a length in the order of 10 m will at high velocities always be relatively blunt. Nevertheless it is suggested to investigate the influence of the hull shape on the wave height and creation of turbulence.
- **Return current jets**. When multiple hulls are towed around in a circular basin, the water in the basin will eventually start to rotate itself, since the moving hulls are a constant supply of momentum. The interaction between the added energy via the hulls and dissipation by the breaking waves, determines the size and location of this current. In the initial design it is suggested to have water jets at the wave pool floor to counteract this effect. The effectiveness as well as the strength and locations of these jets has to be investigated.

A

Derivation of the wave pattern

The wave pattern behind a vessel or an object moving through water has a particular shape consisting of divergent and transverse waves. The deep water wave pattern is derived by Kelvin and is therefore also called the Kelvin wave pattern. This wave pattern has a typical V shape which consists of two interference lines on which interference cusps or featherlet waves are located. In deep water this interference angle θ is circa 20° as proved by **?**. In shallow waters the derivation of the angle of interference θ is more complicated, but analogous to the deep water case. In the following appendix the shallow water case is clarified after reciting the deep water case.

The derivation of the interference angle is as follows:
Consider a ship traveling from Q to O with speed v in time t, in a wide domain with constant water depth h. The ship emits waves all along it's path QO since the bow of the ship acts like a point disturbance and waves of a range of wave lengths radiate out from it. Consider the waves emitted at Q generated a time t before the ship was in O (Figure A.1).

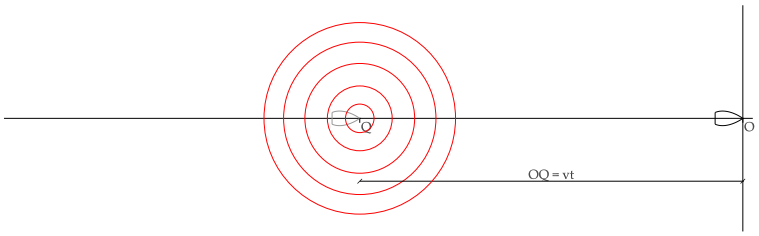

Figure A.1: Waves radiating out from Q a time t before the ship arrived at O.

A.1 Deep water

Step One: Create the canonical crest for an arbitrary wave length λ_i. Let us consider one wavelength λ_i. Waves of this wave length move through the domain with a velocity C_i corresponding with the dispersion relation. Phase speed of waves in deep water only depends on the wave length:

$$C = \sqrt{\frac{g\lambda}{2\pi}}. \tag{A.1}$$

With C, the local phase velocity of the wave [m/s],
λ, the wavelength [m] and
g the acceleration of gravity [m/s^2].
Since waves with this wave length λ_i radiate out in all directions it forms a circular wave with radius $C_i t$. If we draw these circular waves with wave length λ_i for all locations on OQ one straight wave through OR' emerges ('Huygens-principle'). This wave, being the superposition of contributions of all disturbances along OQ with wavelength λ_i, is called the canonical crest (See figure A.2). It moves through the domain with phase speed C_i perpendicular to the crest, and the angle ϕ_i follows from:

$$\phi_i = sin^{-1}(\frac{C_i}{v}). \tag{A.2}$$

The point R_i represents the contribution of the wave from Q to this canonical crest with λ_i.

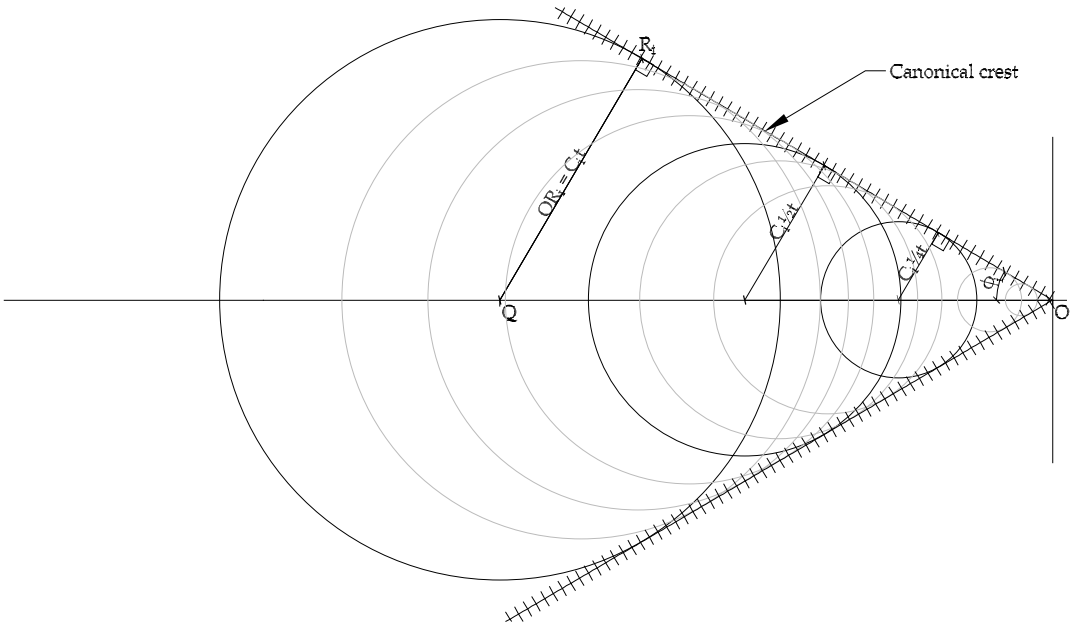

Figure A.2: Step One: Create the canonical crest (+++) for wave length λ_i.

Step Two: Draw all canonical crests and the contribution points R_i. Surely, the bow of the ship does not only emit this wave of length λ_i, it emits a wide range of wavelengths. The canonical crests of for several wave lengths (λ_1, λ_2 ,...,λ_N)are constructed as well as the corresponding points R_1, R_2,...,R_N. Simple geometry proves that all points R_i are on a circle with diameter OQ.

We consider the deep water case, so the wave front travels only at half the phase speed (group velocity $Cg = \frac{1}{2}C$). Positive interference does therefore occur halfway QR_i at point G_i. If all points R_i are on a circle with diameter OQ then all points G_i are on a circle with diameter QM ($\frac{1}{2}$ OQ). This circle around K($\frac{3}{4}$ OQ) represents the interference locations of all wave lengths [1] emitted from Q (see figure A.3). At all other locations in the domain the waves originating from Q do not interfere in a positive way and are therefore hardly in the final wave pattern.

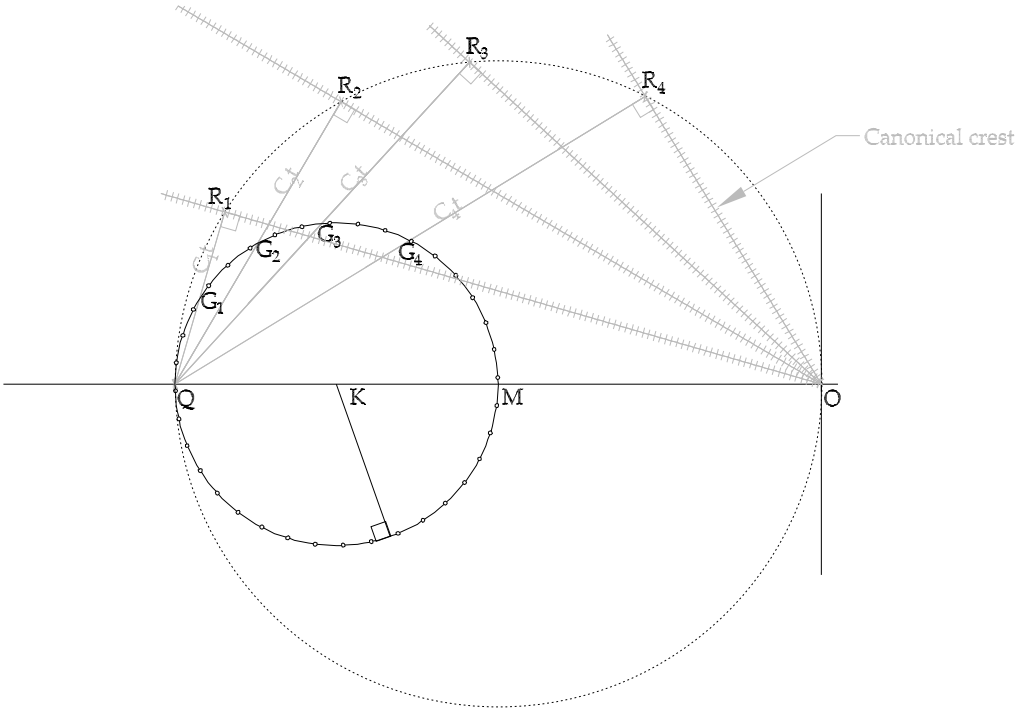

Figure A.3: Step Two: Locations of positive interference for waves emitted at Q , drawn as an arc (-o-) through G_i.

[1] only waves for which $C < v$ are considered for the construction of the wave pattern behind the vessel

Step Three: Construct the interference line The circle just constructed for point Q is to be constructed for all ship locations on OQ (see figure A.4). Maximal positive interference occurs on the tangent along all these circles. The tangent along these circles is therefore the location where the interference cusps are located.

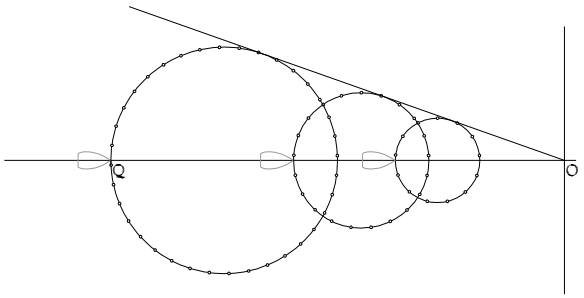

Figure A.4: Step Three: construct the interference line (tangent along interference circles).

Step Four: Calculate angles of featherlet wave and interference line. The angle of the interference line constructed earlier is about 19.5 degrees, which is derived in the following paragraph.
Let OR_i be 1 and $QG_i = G_iR_i$ be a (see figure A.5). Then the following holds:

$$\phi = tan^{-1}(2a), \tag{A.3}$$

$$\theta = tan^{-1}(2a) - tan^{-1}(a). \tag{A.4}$$

The maximum angle of θ equals the angle of maximal interference, and is found by differentiating equation (A.4):

$$\frac{\partial\theta}{\partial a} = \frac{2}{1+4a^2} - \frac{1}{1+a^2} = 0. \tag{A.5}$$

The maximum angle is found at $a = \frac{1}{\sqrt{2}}$, which gives an angle of the interference line θ of 19.47 degrees and a wave angle ϕ of 54.74 degrees.
Substituting and rearranging equations (A.2) and (A.1) gives the wavelength of the featherlet waves:

$$\lambda = \frac{2\pi v^2 sin^2(\phi)}{g} \approx 0.43v^2. \tag{A.6}$$

In between the interference lines the pattern consists of the earlier mentioned transverse and divergent waves. The divergent waves run from the ship position (with a tangent parallel to the sailing line) toward the interference cusps where the tangent is equal to the featherlet wave angle ϕ (see figure A.6). The transverse waves crest is an arc between the two interference cusps. This crest is perpendicular to the sailing line as it crosses this sailing line, ans hence the phase speed of these waves must equal the speed of the vessel. Consequently the following holds:

$$\lambda_t = \frac{2\pi v^2}{g} \approx 0.64v^2. \tag{A.7}$$

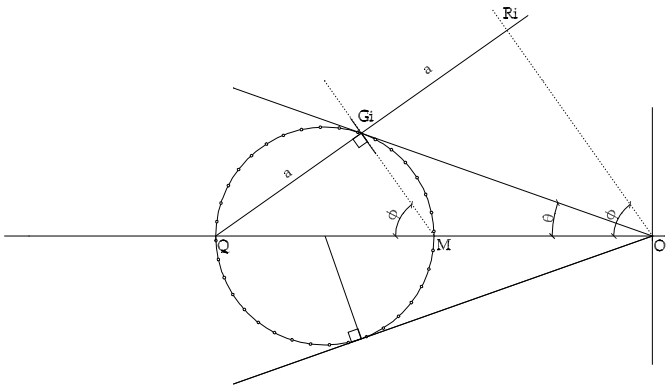

Figure A.5: Wave angle construction.

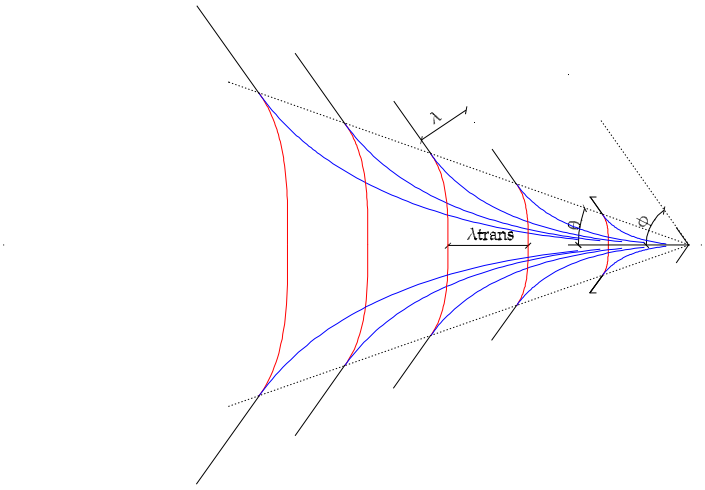

Figure A.6: Full wave pattern in deep water.

A.2 Shallow and intermediate water depths

The derivation of the wave pattern in shallow or intermediate waterdepth is similar to the previous, deep water case. The same steps are taken to compute the pattern, though slightly adjusted.

Step One: Create the canonical crest for an arbitrary wave length λ_i. The difference between deep water and intermediate to shallow waters is that wave characteristics are dependent of the water depth. The canonical wave crest as constructed for deep water is nevertheless identical. The phase speed of waves in intermediate waters is given by:

$$C = \sqrt{\frac{g\lambda}{2\pi} tanh(\frac{2\pi h}{\lambda})}. \tag{A.8}$$

With C, the local phase velocity of the wave [m/s],
λ, the wavelength [m] and
h, the local water depth [m].

Step Two: Draw all canonical crests and the contribution points R_i. Like in deep water, all points R_i (representing the contribution of waves from Q to canonical crests) lie on a circle with diameter OQ.

In deep water we found the actual location of the wave front G_i by dividing OR_i into half as the group velocity is half the phase velocity in deep water. In intermediate waters this ratio between group and phase velocity is:

$$\frac{Cg}{C} \equiv n = \frac{1}{2} + \frac{kh}{sinh(2kh)}. \tag{A.9}$$

With n, the ratio between group and phase velocity [-],
k, the wave number [-] ($\frac{2\pi}{\lambda}$) and
h, the local water depth [m].
The ratio n is dependent on the wave length, varying between 0.5 for relatively deep water to 1 for shallow water. For long waves the water is relatively shallower than for short waves and the ratio n increases with increasing wavelength even with constant water depth h. When constructing the arc through all points G_i (the wave front position) where positive interference occurs the increase of n_i is visible (see figure A.7). The arc through point G_i is described by:

$$x_{Gi} = n_i C_i sin(\phi_i) - OQ, \tag{A.10}$$
$$y_{Gi} = n_i C_i cos(\phi_i). \tag{A.11}$$

With C_i, the phase speed corresponding for a wavelength λ_i [m/s],
n, the ratio between group and phase velocity for a wavelength λ_i[-],
ϕ, the angle of the canonical crest for a wavelength λ_i [-] and
OQ, the distance between emission point Q and the ship O [m] ($= vt$).

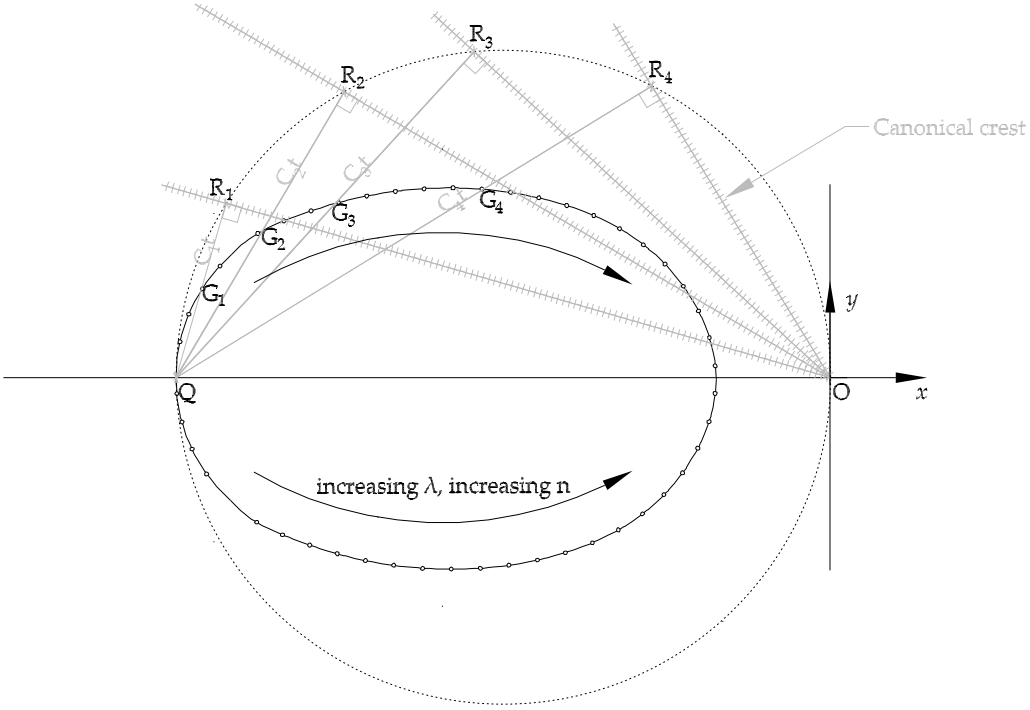

Figure A.7: Step Two: Locations of positive interference for waves emitted at Q , drawn as an arc (-o-) through G_i.

Step Three: Construct the interference line. The arc with positive interference is constructed again for all ship locations on OQ. Positive interference occurs on the tangent along all these arcs and the interference cusps are located on this line. The angle of the interference line depends on the ratio between the wavelengths and water depth, expressed dimensionless as the Froude depth number, $F_{r,d}$ $(=\frac{v}{\sqrt{gh}})$.

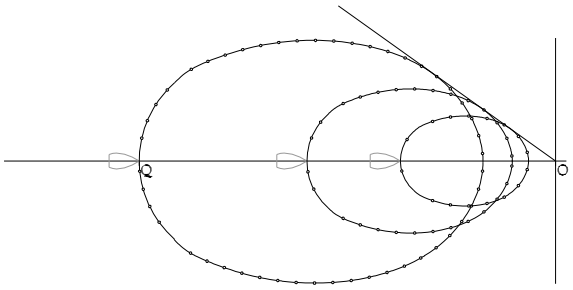

Figure A.8: Step Three: construct the interference line (tangent along interference arcs).

Step Four: Calculate angles of featherlet wave and interference line. The angle of maximal interference is not so elementary as for deep water. The non linear equations (A.8) and (A.9) make differentiating to maximize the angle θ a difficult task. Fortunately

the angles ϕ and θ follow directly from the interference arc given by equations (A.10) and (A.11). The tangent along the arc is found in a graphical presentation (figure A.9), and measured for increasing Froude depth numbers.

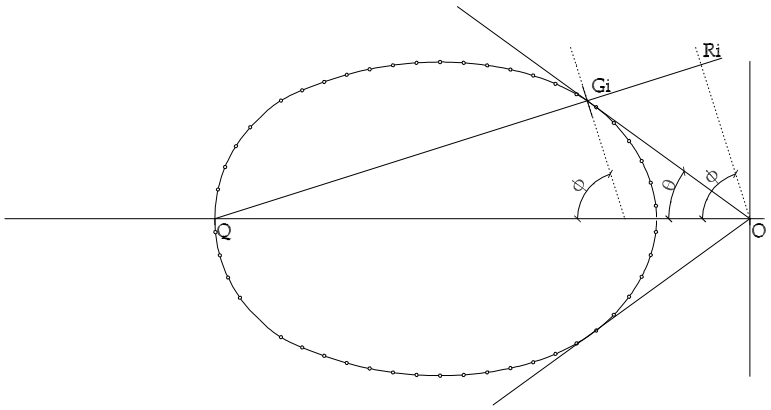

Figure A.9: Wave pattern geometry.

For small Froude depth numbers ($F_{r,d} \leq 0.6$) the water can be considered deep and interference angle and featherlet wave angle are resp 19.47 and 54.74 degrees corresponding to deep water theory. As the Froude depth number further increases beyond 0.6 the angles approach 90 degrees (see figure A.10). Substituting and rearranging equations (A.2) and

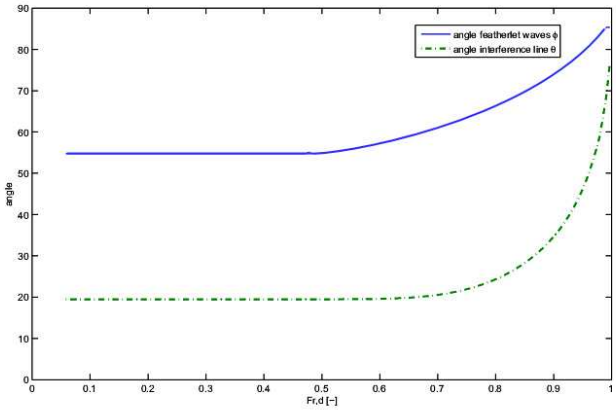

Figure A.10: Computed wave angles as function of $F_{r,d}$
Due to several discretizations in the algorithm finding the featherlet wave angle, the line representing the wave angle is not smooth.

(A.8) gives an implicit equation for the wavelength of the featherlet waves as function of the wavelet angle ϕ:

$$\lambda = \frac{2\pi v^2 sin^2(\phi)}{g} \frac{1}{tanh(\frac{2\pi h}{\lambda})}. \tag{A.12}$$

The transverse wave length can be calculated similar using:

$$\lambda_t = \frac{2\pi v^2}{g} \frac{1}{tanh(\frac{2\pi h}{\lambda_t})}. \tag{A.13}$$

The resulting wave pattern in shallow water is depicted in figure A.11.

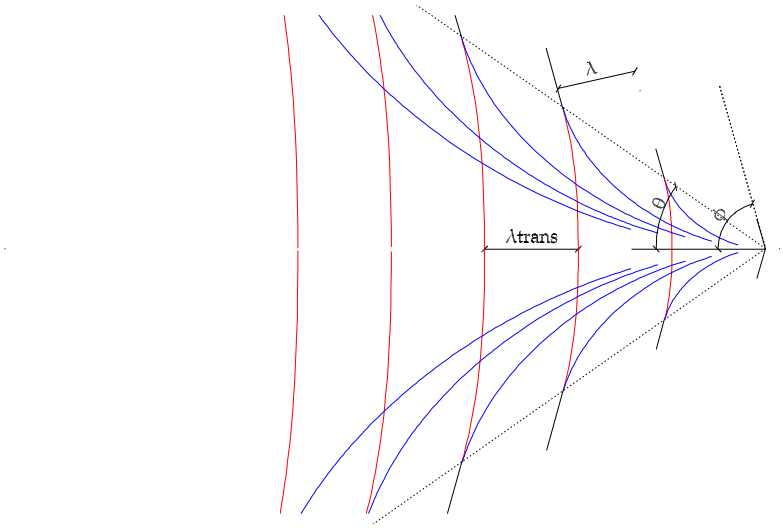

Figure A.11: Full wave pattern for $F_{r,d} = 0.9$.

B

Hull shapes experimental modeling

Hull shapes are based on the most elementary form, a rectangular block. Gradients in the flow generate the secondary wave field and a discrete change in cross section introduces large gradients on a short distance. One of the main purposes of the physical experiment is to produce a dataset for future modeling. Since the sharp edges of a block cause difficulties in numerical models, the rectangular box is slightly rounded off by means of a hyperbolic tangent function (see figure B.1).

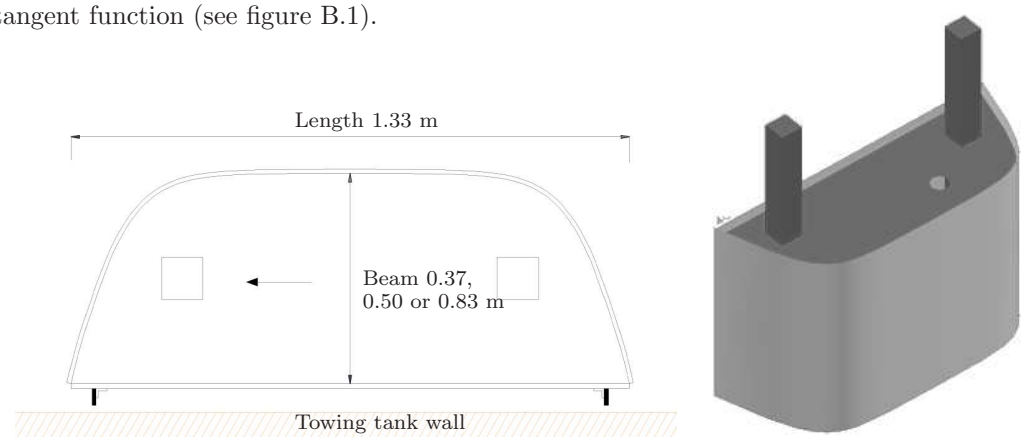

Figure B.1: Top view and 3D view hull shape.

Different hull shapes are towed in the tank, all having a length of 1.33 m and having a beam (width) of 0.37, 0.5 or 0.83 m. Lengths are chosen in the same order as the expected wave lengths. The beams are chosen such that a wide range of blockages from 0.05 to 0.25 can be experimented.

C

Wavelet analysis procedure

The wavelet analysis is a technique to decompose a signal into different features, each having their own timescale. It is particularly useful for signals with a time dependent periodicity, like waves moving through a inhomogeneous velocity field. In a wavelet procedure a short wave, called a wavelet, is compared to the signal. Features of all size are mapped by stretching (scaling) and moving this short wave across the signal. The correlation **C** with the signal is computed for each of these different scales a and positions b of the wavelet. The correlation **C** is computed as follows:

$$\mathbf{C}(\text{scale } a, \text{ position } b) = \int_{-\infty}^{\infty} \frac{1}{\sqrt{a}} \psi\left(\frac{t-b}{a}\right) dt. \tag{C.1}$$

With: a, the scale factor of the wavelet [-],
b, the time shift of the center of the wavelet [s],
$s(t)$, the analyzed signal and
$\psi(t)$, the mathematical description of the wavelet.

The wavelet used in this analysis is derived from a Gaussian probability density distribution, the so-called mexican hat, often used since it has a simple continuous form[1]. The mexican hat wavelet is given by:

$$\psi(t) = \left(\frac{2}{\sqrt{3}}\pi^{-0.25}\right)\left(1-t^2\right)e^{\frac{-t^2}{2}}. \tag{C.2}$$

The function $\psi(t)$ describes a wavelet of finite length, outside the region $-4 \leq t \geq 4$ it is close to zero.

[1] For more background information on different wavelet shapes and their (dis)advantages, the reader is referred to Kaiser (1994)

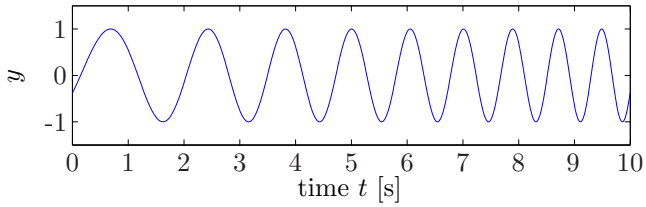

Figure C.1: Analyzed signal $s(t)$

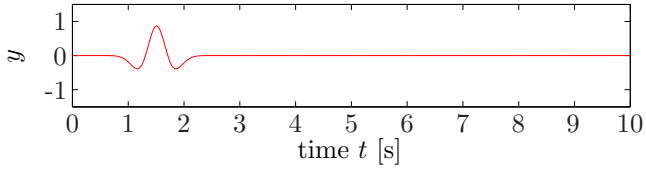

Figure C.2: Mexican hat wavelet ($a_1 = 0.2, b = 1.5$).

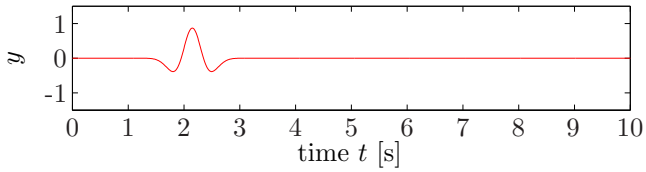

Figure C.3: Mexican hat wavelet ($a_1 = 0.2, b = 2.1$).

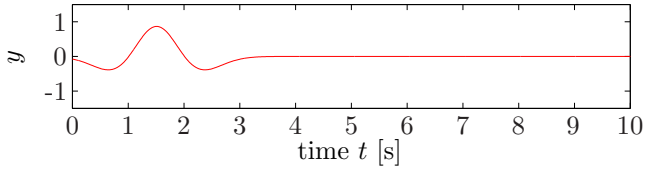

Figure C.4: Mexican hat wavelet ($a_2 = 0.5, b = 1.5$).

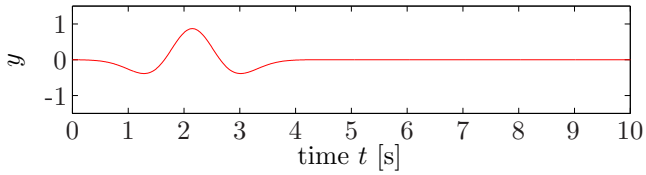

Figure C.5: Mexican hat wavelet ($a_2 = 0.5, b = 2.1$).

The wavelet procedure is clarified hereunder by a simple example.
Consider a signal with a time dependent period (figure C.1). The 'mexican hat' wavelet is scaled with a_1 and shifted with varying b across the signal (figures C.2 and C.3). For each timeshift b the correlation [C] between the signal and the wavelet is calculated. Locations with high C values the wavelet form have a high resemblance with the signal.
Once the whole signal has been evaluated with the wavelet of scale a_1, the scale of the wavelet is increased to a_2 and compared to the signal once again over the whole time domain (figures C.4 and C.5).
The correlation values are mapped in a scaleogram, where lighter colors indicate a high correlation. The scaleogram for a wavelet analysis using only two scales, a_1 and a_2, is shown in figure C.6. From the scaleogram it can be read that a wavelet with scale $a_1 = 0.2$ resembles quite well around $t = 8s$, wheras the wavelet with scale $a_2 = 0.5$ resembles the beginning of the signal.
For a physical meaning the scales a are converted to pseudo periods T by multiplying by the center period T_c of the wavelet, $T = T_c a$. The center period T_c is the period of a sinusoidal function with the maximum correlation with the unscaled wavelet. In other words, a sinusiodal function with period T_c will represented best by a wavelet with scale $a = 1$. For the 'mexican hat' wavelet the center period T_c equals 4 s.
Hence the scales a_1 and a_2 correspond to pseudo periods $T_1 = 0.8s$ and $T_2 = 2s$.

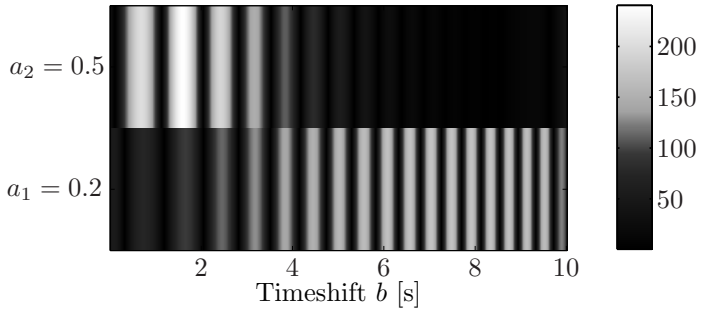

Figure C.6: Scaleogram wavelet analysis with 2 scales, lighter colors indicate a high correlation.

When the wavelet analysis is performed with a continuous scale range the scaleogram maps the different periods in the signal more accurate (figure C.7).

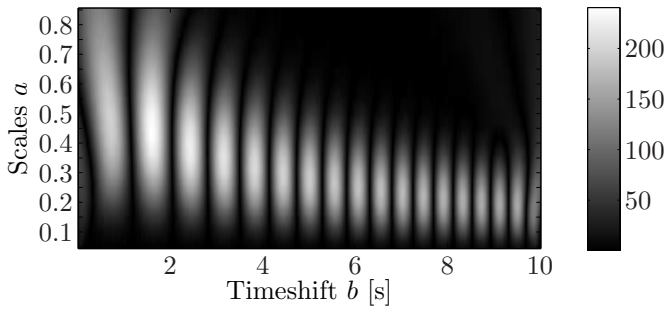

Figure C.7: Scaleogram wavelet analysis with continuous scale range, lighter colors indicate a high correlation.

Bibliography

Battjes, J.A., (1974). *Surf Similarity.* Proceedings 14th International Conference on Coastal Engineering, pp. 467-479. Kopenhagen.

Dally, W.R. (2001). *Improved Stochastic models for Surfing Climate.* Journal of Coastal Research, SI(29), 41-50. CERF; Florida.

Havelock, T.H, (1908). *The Propagation of Groups of Waves in Dispersive Media with Application to Waves on Water Produced by a Travelling Disturbance.* Proceedings of the Royal Society, Series A, Vol LXXXI, pp 398. 430. London.

Henriquez, M. (2004). *Artificial Surfing Reefs.* MSc. Thesis, Delft University of Technology; Delft.

Huang, N.E., Shen, Z., Long, S.R., Wu, M.C., Shih, H.H., Zheng, Q., Yen, N., Tung, C.C. and Liu, H.H. (1996). *The empirical mode decomposition and the Hilbert Spectrum for nonlinear and non-stationary time series analysis.* Proceedings of the Royal Society, pp. 903-995. London.

Hutt, J.A., Black, K.P. and Mead, S.T. (2001). *Classification of Surf Breaks in Relation to Surfing Skill.* Journal of Coastal Research, SI(29), 66-81, CERF; Florida.

Jansen, P.Ph. and Schijf, J.B. (1953). *Influence on the form and dimensions of the cross section of the canal, of the form, of the speed, and the propulsion system of vessels.* Proceedings XVIIIth International Navigation Congress; Rome.

Kaiser, G (1994). *A friendly guide to wavelets.* Birkhauser; Boston.

Koning Gans de, H (1992). *A higher order panel method for potential flow around an arbitrary body.* Delft University of Technology; Delft.

Lamb, H (1932). *Hydrodynamics.* Cambridge University Press; Cambridge.

Lap, A.J.W. (1954). *Fundamentals of ship building and propulsion.* International Shipbuilding Progress; Rotterdam.

Lighthill, J. (1978). *Tracts in mathematics and mathematical physics.* Cambridge University Press; Cambridge.

Maritime and Coastguard Agency (2001). *Res. Proj. 457 A Physical Study of Fast Ferry Wash Characteristics in Shallow Water.* The Maritime and Coastguard Agency; Belfast.

Mei, C.C. (1989). *The applied dynamics of ocean surface waves.* World Scientific; Singapore.

Stive, M.J.F. (1984). *A scale comparison of waves breaking on a beach.* Coastal Engineering, 9, pp 151-158. Elsevier Science Publishers B.V.; Amsterdam.

Stoker, J.J. (1957). *Water waves; The mathematical theory with applications.* Interscience Publishers; New York.

Verheij, H.P. and Bogaerts, M.P. (1986). *Sekundaire scheepsgolven en hun invloed op taludbekleding.* Verslag modelonderzoek M1115 deel VI, Delft Hydraulics; Delft.

Vries, de S. (2007). *On the generation of surfable ship waves in a circular pool: Part II; the application of stereo photo technique measuring water surface elevation and surface flow velocities.* MSc. Thesis, Delft University of Technology; Delft.